Enhanced asymmetric supercapacitor device performance of graphene templated β-$Bi_{2-x}Eu_xMo_2O_9$ nano self-assembly

Jesman Sthevan Kovil Pitchai [a], *Bagavathy Shunmughananthan* [b], *Priyadharshini Shanmugam* [b], *Govarthini Seerangan Selvam* [b], *Alagar Muthukaruppan* [c], *Thangaraju Dheivasigamani* [b*], *Sivakumar Periyasamy* [a*]

[a]*Solid State Ionics Lab, PG & Research Department of Physics, Thanthai Periyar Government Arts and Science College (Autonomous), (Affiliated to Bharathidasan University), Tiruchirappalli-620023, Tamil Nadu, India*

[b]*Nano-crystal Design and Application Lab (n-DAL), Department of Physics, PSG Institute of Technology and Applied Research, Coimbatore-641062, Tamil Nadu, India*

[c]*Polymer Engineering Lab (PEL), Departmet of Chemistry, PSG Institute of Technology and Applied Research, Coimatore-641062, Tamil Nadu, India.*

***Corresponding author.**

E-mail address: dthangaraju@gmail.com (Thangaraju Dheivasigamani)

E-mail address: sivakumarpsk72@gmail.com (Sivakumar Periyasamy

Abstract

The electrode material plays a crucial role in the performance of energy storage devices. Currently, the research focuses on enhancing the super-capacitive nature of the existing electrode materials in many ways. Herein, the influence of rare earth ions in the electrochemical characteristics of β-$Bi_{2-x}Eu_xMo_2O_9$ and graphene-modified GrM-β-$Bi_{2-x}Eu_xMo_2O_9$ is investigated. The gel matrix method is adopted for synthesizing the $Bi_{2-x}Eu_xMo_2O_9$ (x = 1, 5 and 10%) and GrM - $Bi_{2-x}Eu_xMo_2O_9$ (x = 5,10%). The as-synthesized material's structural formation, phase purity and structural modifications are studied using XRD, Raman and SEM. The chemical composition with their oxidation state is verified using XPS analysis. The electrochemical behavior of the pristine materials is examined with various analyses such as CV, GCD and EIS techniques in both three-electrode and two-electrode systems. The specific capacitance of GrM-$Bi_{1.8}Eu_{0.2}Mo_2O_9$ is 904 F g^{-1} at 1 A g^{-1} with excellent cyclic stability of about 82.14% at 5 A/g after 5000 cycles. An ASC device developed using GrM-$Bi_{1.8}Eu_{0.2}Mo_2O_9$ exhibits columbic efficiency of 96.5% with an extended cyclic life of 76.9% after 10000 cycles. The fabricated device possesses energy density and power density of 60.21 W h K g^{-1} and 750 W K g^{-1}, respectively, at 1A g^{-1}, acting as a favorable candidate for supercapacitor application.

Keywords: Bismuth molybdate, supercapacitor, Graphene modification, asymmetric device.

1. Introduction

The world echoes the appeal to save energy essential to our everyday existence. As our current nonrenewable energy sources continue to dwindle, scientists and engineers are working hard to create alternative energy sources, energy-storing materials, and efficiency enhancements.[1–3] In this way, several studies are being done to enhance the performance of energy-storing elements. From the findings of the vibrant researchers, high-efficiency energy storage technologies, including batteries and eco-friendly supercapacitors, can be employed to store and utilize the harvested energy wisely.[4] However, the energy market is currently dominated by batteries. Nevertheless, looking for an alternative energy system that is on par with or even better than batteries is dynamic.[5–7] This opens the way for a flurry of research into generally available, low-cost energy storage technologies with good electrochemical characteristics. In particular, supercapacitors have been a center of attraction over the modern decades since they have a superior power density, an extended cycle life, identical trustworthiness, and a fast rate of charge and discharging capability. Without a doubt, the invention of supercapacitors has helped the development of alternate ways to store energy.[8–10]

The effectiveness of a supercapacitor is determined by its electrode material, electrolyte, and assembly configuration.[11] Among these, the material utilized for the electrodes is one of the most significant components of a supercapacitor.[12] Electric double-layer capacitance (EDLC) is a way that the double-layer effect is used to save energy. Although no charge is transferred, electrostatic induction induces charge at the electrode interface. They have greater power densities and a long lifespan. However, they do not have efficient specific capacitance and energy density to meet the needs of electric vehicles for peak power support.[13,14] By storing energy via interfacial reversible faradaic processes, pseudocapacitive materials significantly

enhance supercapacitors' specific capacitance and energy density compared to carbon-based materials.[15] Combining electric double-layer capacitive materials with pseudocapacitive materials can further improve energy and power density in asymmetric supercapacitors.[16]

Herein, nanostructured transition metal oxides (TMO) are preferable for high-performance supercapacitor electrodes. Because they are environmentally friendly, inexpensive, have high theoretical capacitance, and are widely available.[17,18] In recent years, TMOs have been the focus of research in preparation for their prospective application as electrodes in supercapacitors.[19–22] However, TMOs have a variety of limitations that make them less useful, such as slow ion diffusion, poor electrochemical stability, and low electrical conductivity. In contrast, binary metal oxides have been used as electrode materials to solve these problems because of their many oxidation states for redox processes that aid in the electrical conductivity and the specific capacitance.[23–25]

As such, bismuth molybdate is an important family member of binary metal oxides because it has great electrical and optical properties. Bismuth molybdate has been employed in various sectors, such as catalysts, gas sensors, and energy storage devices. Since then, bismuth molybdate's exceptional supercapacitive behavior has garnered much attention in supercapacitors.[26–32] When applied to binary metal oxides, conducting polymers and carbon-active chemicals can improve their electrochemical performance and specific capacitance as they posses high electrical conductivity, large specific surface area, and extremely long cycling life.[33–35] Similarly, carbon-based materials and conducting polymers have done amazing things in supercapacitor applications.[36–39] At the same time, compared to polymers, carbon compounds are cheaper and occur more often in nature. As a result, researchers have concentrated on optimizing bismuth

molybdate electrode materials by including carbon active material to improve specific capacitance and other electrochemical parameters for usage in supercapacitors.[40,41] We have previously reported the wasp nest M-$Bi_2Mo_2O_9$ on this path, which has a specific capacitance of 831 Fg^{-1} at a scan rate of 1 A g^{-1}.[42] In addition, we have made much progress with carbon-active binary metal oxides that have been enhanced with rare earth elements.

Here, we use a gel matrix approach to create a nano assembly of europium mixed with $Bi_2Mo_2O_9$ and those materials modified with graphene. The Gel matrix method yields more homogeneous particles at lower temperatures than conventional hydrothermal and wet chemical synthesis techniques. This gel matrix technique helps achieve a single-phase nanoparticle formation.[43] Synthesized nanocomposites were used to create the working electrode. The electrochemical nature and cyclic stability of the designed electrode were analyzed to see if they could be used in a high-energy symmetric supercapacitor. Although it has potential as a supercapacitor material, $Bi_2Mo_2O_9$ is rarely discussed. In response, europium-doped graphene-modified $Bi_2Mo_2O_9$ (GrM-$Bi_{2-x}Eu_xMo_2O_9$) based asymmetric high-energy supercapacitors were developed.

2. Experimental section

2.1. Materials

Europium (III) oxide (Eu_2O_3), bismuth(III) nitrate pentahydrate ($Bi(NO_3)_3.5H_2O$), nitric acid (HNO_3), citric acid monohydrate ($C_6H_8O_7.H_2O$), and ammonium heptamolybdate tetrahydrate ($(NH_4)_6Mo_7O_{24}$) were all supplied by Merck. Ethylene glycol ($C_6H_6O_2$) was procured from Himedia. All of the materials employed in this work were used any purification.

2.2. Synthesis

The gel matrix technique was used to generate the $Bi_2Mo_2O_9$ nano self-assembly. The following procedures ensured that the synthesis would go off without a hitch. 1.75 mmol of bismuth (III) nitrate pentahydrate ($Bi(NO_3)_3.5H_2O$), 0.0175 mmol of europium (III) nitrate hexahydrate ($Eu(NO_3)_3.6H_2O$), 0.25 mmol of ammonium $(NH_4)6Mo_7O_{24}$, and 2 mmol of citric acid monohydrate ($C_6H_8O_7.H_2O$) were employed in this route. $(NH_4)_6Mo_7O_{24}$ is stirred separately in 45 mL of distilled water, and the Bi $(NO_3)_3.5H_2O$ in 5 mL of acetic acid. The prepared solution was mixed and stirred for an hour to ensure it was completely combined. The solution was then gelled by adding a measured amount of citric acid and a few drops of ethylene glycol.[44–47] On a temperature-controlled hotplate, the previously described gel solution was heated to 80 °C. Furthermore, the obtained gel was pre-heated at 300 °C to initiate the combustion reaction. Furthermore, recovered samples were reheated at 550 °C to remove organic compounds and achieve the $Bi_{2-x}Eu_xMo_2O_9$ phase. The same synthesis protocol was used to create $Bi_{2-x}Eu_xMo_2O_9$ with varying concentrations of europium (x = 1, 5 and 10 %) and graphene-modified Eu doped $Bi_2Mo_2O_9$ (GrM- $Bi_{2-x}Eu_xMo_2O_9$) (x = 5,10%) by adding rGO. The synthesized product was used for all subsequent characterizations.

2.3. Electrode preparation

In our three-electrode setup, the reference electrode (RE) was made of Ag/AgCl, the counter electrode (CE) was made of Pt wire, and the working electrode (WE) was made of the synthesized active material. For the working electrode, a homogenous mixture was made by blending PVDF (5%), activated carbon (10%), and active material (85%) in a solvent (NMP) N-Methyl-2-pyrrolidinone. After coating a 1 cm^2 (1x1 cm) square of Ni-foam with the produced

slurry, the square was heated to 70 °C and kept there for 12 hours. For use with a two-electrode configuration, activated carbon (AC) was the negative electrode, whereas the positive electrode was composed of annealed Eu-doped $Bi_2Mo_2O_9$ nanostructures. The cellulose membrane also serves as a separator between the electrodes, allowing ions to pass through. The results of CV, GCD, and EIS experiments were used to examine the electrochemical performance of the annealed $Bi_{2-x}Eu_xMo_2O_9$ (x = 1, 5 and 10%) and GrM - $Bi_{2-x}Eu_xMo_2O_9$ (x = 5,10%) in the three-electrode configuration and the two-electrode device with 3M KOH electrolyte.

2.4. Instrumentation:

Using powder X-ray diffraction (PXRD, Rigaku, Japan) with a 2θ range of 10° to 90° and a scan rate of 2°/min, the phase purity of prepared nanoparticles can be determined. We evaluated the as-synthesized materials for Raman spectral analysis at 532 nm excitation with a Horiba Jobin Yvon HR 800 Raman spectrometer. For analyzing the optical absorption and reflection of the chemical components, diffuse reflectance imaging with Thermofisher UV-visible spectrophotometers was used. A ZEISS EVO 18 scanning electron microscope (SEM) examined the morphology and elemental distribution. Further, the detailed growth pattern and the morphology were confirmed using JEOL Japan, JEM 2100 Plus transmission electron microscope (TEM). The Thermo Scientific K-Alpha Surface Investigation with Al Source was used for X-ray Photoelectron Spectroscopy (XPS) analysis of each Eu: $Bi_2Mo_2O_9$ phase. CV, GCD, and EIS's electrochemical properties were studied with the help of an electrochemical workstation. (BioLogic SP-150).

3. Results and discussion

3.1. Structural Studies

The schematic illustration of synthesized materials for supercapacitor application is shown in Figure 1. X-ray diffraction is the most reliable method for determining a material's structure, lattice parameters, and phase purity (XRD). Figure 2 depicts the diffraction patterns of (1, 5, 10%) Eu: $Bi_2Mo_2O_9$ and (5, 10%) Eu: GrM - $Bi_2Mo_2O_9$. The β-$Bi_2Mo_2O_9$ exhibits a monoclinic structure with the space group of P21/n and lattice parameters a = 11.9720, b = 10.8130, c = 11.8990. The diffraction patterns of β- $Bi_2Mo_2O_9$ correlate with the standard JCPDS data, confirming the formation of single phase β-$Bi_2Mo_2O_9$ without impurities. The intense characteristic peak at 2θ = 27.7 corresponds to the (320) plane and does not exhibit a noticeable difference in intensity on the addition of Eu^{3+} ions. The double-shouldered peak at 2θ = 28.11º of β-$Bi_2Mo_2O_9$ disappears with further incorporation of rare earth ions. The magnified spectrum of intense peak at 27.7 2θ of pure $Bi_2Mo_2O_9$ and 1, 5, and 10% Eu doped $Bi_2Mo_2O_9$ is shown in Figure S1. The Eu doped $Bi_2Mo_2O_9$ results in slight shift of peak towards higher angle. While, the 5 and 10% Eu doped $Bi_2Mo_2O_9$ shifted back towards lower angle from 1% Eu doped $Bi_2Mo_2O_9$. This may due to more availability of Eu^{3+} ions in $Bi_{1.9}Eu_{0.1}Mo_2O_9$ and $Bi_{1.8}Eu_{0.2}Mo_2O_9$ than $Bi_{1.98}Eu_{0.02}Mo_2O_9$, resulting in site adaption of Eu^{3+} in $Bi_2Mo_2O_9$.

3.2. Raman Spectral Analysis

Raman spectroscopy is utilized to ascertain materials' rotational, vibrational, and molecular states in their as-synthesized state. Figure 3 shows the Raman spectrum of prepared materials. The strong peak appeared at 888 cm^{-1}, attributed to the Mo–O stretching vibrations of orthorhombic distorted MoO_6 octahedra. The Mo-O bonding modes, such as bending, twisting, and wagging, contribute to peaks below 600 cm^{-1}, while Mo-O stretches account for peaks above 600 cm^{-1}. Minor peaks at 146 cm^{-1}, 287 cm^{-1}, and 366 cm^{-1} also indicate the formation of $Bi_2Mo_2O_9$.[48]. The modes below 205 cm^{-1} correspond to the conversion of Bi and Mo atoms.[49] The hump

around 749 cm-1 for $Bi_2Mo_2O_9$ gradually gets intense by doping Eu^{3+} ions and further becomes sharp peak for GrM- $Bi_{1.8}Eu_{0.2}Mo_2O_9$. Also, the doping of europium ions results in the shift of peak appearing at 197 cm-1 for $Bi_2Mo_2O_9$ and becoming intense at 204 cm^{-1} for GrM-$Bi_{1.8}Eu_{0.2}Mo_2O_9$. The Raman spectrum of 825 to 950 cm^{-1} is given in Figure S2. The slight increasing shift of Raman spectrum is observed for $Bi_{2-x}Eu_xMo_2O_9$ (x = 1, 5 and 10%). Also, the addition of graphene to 5 and 10% Eu doped $Bi_2Mo_2O_9$ doesn't show significant changes in their corresponding Raman spectrum as the graphene gets destructed at high annealing temperature.

3.3 XPS Analysis

The chemical constituents of the synthesized materials were analyzed using XPS analysis. Figure 4 (a) depicts the survey spectrum of $Bi_{1.8}Eu_{0.2}Mo_2O_9$ and GrM-$Bi_{1.8}Eu_{0.2}Mo_2O_9$ ranging from 1400 eV to 0 eV, assuring the presence of Bi, Mo, O, and Eu thereby confirming the effective formation of the material without any impurities present. The two definite peaks observed from the Bi 4f spectrum (Figure 4(b)) of $Bi_2Mo_2O_9$ centered around 165 eV and 159 eV corresponds to Bi $4f_{5/2}$ and Bi $4f_{7/2}$, respectively. A small shift in the peak is observed in the Bi 4f spectrum of 10% Eu: $Bi_2Mo_2O_9$ and 10 % Eu: GrM- $Bi_2Mo_2O_9$.[50] The binding energies for the intense peaks of Mo $3d_{3/2}$ and Mo $3d_{5/2}$ is located at 235 and 232.7 eV, respectively (Figure 4(c)). Due to Eu doping and graphene modification, Mo $3d_{3/2}$ and Mo $3d_{5/2}$ peaks shift to binding energy around 236 and 233 eV. The findings from the Bi 4f spectrum and Mo 3d spectrum affirm the oxidation state of (Bi^{3+}) and molybdenum (Mo^{6+}).

The high-resolution O 1s spectrum (Figure 4(d)) indicates the characteristics peak at 530.8 eV and 531.3 eV for $Bi_2Mo_2O_9$ and GrM-$Bi_{1.8}Eu_{0.2}Mo_2O_9$ owing to Bi-O and Mo – O bonds. [51–53] The Eu 3d spectrum (Figure 4(e)) comprises the peak at 1135.5 eV attributed to Eu $3d_{5/2}$, indicating the presence of Eu^{3+} ions.[47] The C 1s peak at 285 eV from Figure 3(f) shows the small

amount of natural carbon in the prepared samples. Thereby, it confirms the absence of rGO in thermally treated synthesized materials. The UV–visible analysis was carried out, and the relevant discussions were provided in the supporting information (Figure S3).

3.4 Morphological Analysis using FE SEM

The surface morphology and structural modifications by the effect of Eu^{3+} ions in $Bi_2Mo_2O_9$ were corroborated using SEM. Figure 5 depicts the SEM micrographs of $Bi_2Mo_2O_9$ (a-d), $Bi_{1.98}Eu_{0.02}Mo_2O_9$ (e-h), $Bi_{1.9}Eu_{0.1}Mo_2O_9$(i-l), $Bi_{1.8}Eu_{0.2}Mo_2O_9$ (m-p), GrM-$Bi_{1.9}Eu_{0.1}Mo_2O_9$ (q-t) and GrM-$Bi_{1.8}Eu_{0.2}Mo_2O_9$ (u-x). The SEM images of $Bi_2Mo_2O_9$ reveal the nest-shaped formation of materials with thin-edged walls. The sphere shape and extended tube-like particles seem to be embedded together. The formation of the interconnected framework structures has been noticed for the as-synthesized samples. The surface of the particles appears to have several porous structures that developed perpendicular to it. The growth of layered inner microporous structures has been observed on further magnification. The SEM images of $Bi_{2-x}Eu_xMo_2O_9$ show that the particles are broken spheres without adding rGO. The regulated growth of GrM-$Bi_{2-x}Eu_xMo_2O_9$ may be due to rGO, which acts as a template. The nest-like form increases surface area, thereby helping in improving electrochemical behavior. In addition, the thin walls and the particles' tightly stacked arrangement will enhance ionic transport. The elemental confirmation of the synthesized materials was confirmed using EDAX (Figure S4) and the elemental weight percentage of the synthesized samples are included in the supporting information (Table S1).

3.5 TEM analysis

The electrochemical performance of a material can also be influenced by its morphology. Therefore, the detailed growth of as-synthesized electrode material is studied using TEM and shown in Figure 6. The visibility of the lattice fringes confirms the crystallinity nature of the

synthesized materials. The TEM image of GrM-$Bi_{1.8}Eu_{0.2}Mo_2O_9$ shows the lattice fringe with an interplanar spacing of 3.33 Å that corresponds to the plane (-131). The smooth edges of GrM-$Bi_{1.8}Eu_{0.2}Mo_2O_9$ indicate regulated growth development. From TEM analysis, it is evident that rGO acts as a template for the growth of $Bi_{1.8}Eu_{0.2}Mo_2O_9$, resulting in the formation of sheets-like structures.

3.6 BET Analysis

Brunauer-Emmett-Teller (BET) analysis was used to investigate the surface area and pore size distribution of the synthesized sample and it is shown in Figure 7. The resulting BET isotherm shows a characteristic type IV hysteresis loop, which suggests that the particles have a mesoporous structure. The surface area of $Bi_2Mo_2O_9$, $Bi_{1.8}Eu_{0.2}Mo_2O_9$ and GrM-$Bi_{1.8}Eu_{0.2}Mo_2O_9$ are 15.087, 20.961, and 26.128 m^2/g, respectively. The comparision of surface area, pore size, and pore volume of $Bi_2Mo_2O_9$, $Bi_{1.8}Eu_{0.2}Mo_2O_9$ and GrM-$Bi_{1.8}Eu_{0.2}Mo_2O_9$ was tabulated (Table 1). From BET analysis it is evident that graphene acts as template for the growth of the nanoparticles thereby enhancing the surface area.

3.7 CV Analysis

The electrochemical behavior of $Bi_{2-x}Eu_xMo_2O_9$ (x = 1, 5 and 10%) and GrM-$Bi_{2-x}Eu_xMo_2O_9$ (x = 5 and 10%) sample electrodes was investigated in comparison with pure $Bi_2Mo_2O_9$ using three-electrode system and a 3M KOH electrolyte solution. As in Figure 8 (a-f), these samples were first tested using cyclic voltammetry (CV) in the potential range of 0–0.5 V at a scan rate of 5–100 mV/s. Redox features in all CV curves support the electrodes' pseudocapacitive behavior.[54] By sweeping the scan rate, the corresponding current densities of these electrodes increased, indicating that they were capacitive and stable in charge storage. Because the cathodic and anodic peaks have shifted to the lower and higher potential sides, doped

samples have higher charge and discharge rates than pure samples.[55] The CV curves of any of the electrodes show no discernible distortion. The GrM-$Bi_{2-x}Eu_xMo_2O_9$ nanocomposite electrode has a larger integral surface area than the $Bi_{2-x}Eu_xMo_2O_9$-based electrode. This might arise from the formation of oxygen vacancies when Eu ions are exchanged for $Bi_2Mo_2O_9$ sites, resulting in a narrower band gap with greater electrical conductivity.[56] Along with the benefits of fast ionic movement, decreased ion transfer distance, and a smaller band gap, rapid transitions of Eu ions between the Eu^{2+} and Eu^{3+} states are noteworthy. Compared to the pure electrode, the GrM-$Bi_{2-x}Eu_xMo_2O_9$ nanocomposite electrodes' specific capacitance is increased. Furthermore, incorporating Eu ions at sites on $Bi_2Mo_2O_9$ improves the composite's interfacial contact. Thus, the integral surface area of the GrM-$Bi_{2-x}Eu_xMo_2O_9$ nanocomposite electrode is greater than that of other electrodes.[57]

The Trasatti approach was also used to classify and study an electrode material's intrinsic charge storage properties. The method proposed by Trasatti et al. aids in estimating the contributions of the diffusion (inner) and surface controlled (outer surface) to the total charges approximately using cyclic voltammograms. The underlying concept is that the charged species on the inner surface adopts a diffusion-controlled method, wherein the electrode's outer surface follows a non – diffusion controlled route irrespective of scan rate.[58,59] Figure 9 shows the bar graph comparison displaying the faradic and capacitive contributions of the prepared electrode materials, and the linear plots are provided in the supporting information (Figure S5 and S6). It is evident from the graph that the GrM-$Bi_{1.8}Eu_{0.2}Mo_2O_9$ based electrode exhibits a charge of about 78.16 % associated with faradaic effects and the rest 21.4 % by capacitive effects.

3.8 EIS Analysis

Electrochemical impedance spectroscopy (EIS) was investigated in a 3M KOH electrolyte solution over a frequency range of 0.01 to 100 kHz on the manufactured composite electrodes. The Nyquist plot of the manufactured electrodes is displayed in Figure 10. We used this fitted equivalent circuit C1/(R1+C2/R2+M3) to determine the ohmic drop, the displacement of charged ions across the electrode mass interface, and the constant phase components of the cell resistance. According to these equivalent circuit fitting results, the $Bi_{2-x}Eu_xMo_2O_9$ composite electrodes and the GrM-$Bi_{2-x}Eu_xMo_2O_9$ composite electrodes had the lowest solution resistances (Rs). Moreover, the prepared electrodes' charge transfer resistances (Rct) are determined and listed in Table 1. Figure 10 shows that an equivalent circuit for the EIS has been constructed (C). Compared to other electrodes, the GrM-$Bi_{2-x}Eu_xMo_2O_9$ electrode has a higher capacitance due to its small crystalline size, low band gap energy, and high electrical and ionic conductivities, as shown by the EIS results.[42,60,61] Analytically, the EIS findings are highly correlated with the CV findings. The GrM-$Bi_{2-x}Eu_xMo_2O_9$ electrode shows marked improvement in electrochemical performance, as shown by the results. The interfacial contact between the Bi and Mo was enhanced by adding Eu to the graphene-modified $Bi_2Mo_2O_9$ matrix. The electrochemical reaction is consequently triggered by the decreased band gap and increased electrical conductivity of $Bi_2Mo_2O_9$ brought about by Eu doping and graphene modification.[62–64]

3.9 GCD Analysis

The prepared $Bi_{2-x}Eu_xMo_2O_9$ and GrM-$Bi_{2-x}Eu_xMo_2O_9$ electrodes were employed for a galvanostatic charge-discharge (GCD) study at a current density of 1 to 5 A g^{-1} and a potential range of 0 to 0.5 V. Figure 11 depicts the GCD curves of $Bi_{2-x}Eu_xMo_2O_9$ (x = 1,5 and 10%) and GrM-$Bi_{2-x}Eu_xMo_2O_9$ (x = 5 and 10%). The small iR drop and the nonlinearity curve in the discharge demonstrated that the prepared electrodes were battery-type. Discharge times are longer

for low current densities compared to high current densities. Also, the charging and discharging times are longer and shorter at lower and higher current densities. The ion exchange process works well at low current densities. Because ion movement is slow at low currents, redox reactions can occur throughout the active material, resulting in a higher capacitance. However, the ions do not have enough time to undergo a redox reaction over the entire area of the active material when the current density is increased. As a result, the capacitance of the electrodes will be reduced.[65–67]

The relation enumerates the specific capacitance (C) from the GCD curve.

$$C = \frac{I \times \Delta t}{m \times \Delta V} \; Fg^{-1} \qquad (1)$$

Where ‘‘I’’ represents the current density (A),

‘‘Δt’’ stands for the discharge time (s) from the Galvanostatic charge-discharge curve,

‘‘m’’ is the mass of the active material (g) deposited on the electrode surface and

‘‘ΔV’’ is the applied voltage window (Volts)

Calculated specific capacitances at different current densities for the $Bi_{2-x}Eu_xMo_2O_9$ (x = 1,5 and 10%) and GrM-$Bi_{2-x}Eu_xMo_2O_9$ (x = 5 and 10%) composite electrodes are tabulated. The GCD result shows that doping GrM-$Bi_{2-x}Eu_xMo_2O_9$ composite with Eu ions enhances its supercapacitance performance, leading to greater specific capacitance and superior cycle stability. Values for specific capacitance calculated for current densities up to 5 A g^{-1} are provided in the supporting information (Table S2). It has been found that the specific capacitances gradually decrease with increasing current density. The modified graphene and Eu ions boost electronic and ionic conductivities, making the OH^- ions more accessible by creating more active sites. As a result, capacitance is increased in GrM-$Bi_{1.8}Eu_{0.2}Mo_2O_9$ electrode composites. Figure 12(a) shows how the current density relates to the specific capacitance.[68,69]

Regarding CV, GCD, and EIS measurements, the GrM-$Bi_{1.8}Eu_{0.2}Mo_2O_9$ electrode performed better. Thus, we looked at the cycle stability of the same electrode in GCD for an additional 5000 cycles. At a current density of 5 A g^{-1} and a potential window of 0 – 0.5 V, the capacitance retention of the GrM-$Bi_{1.8}Eu_{0.2}Mo_2O_9$ composite electrode was 82.14%, as shown in Figure 12(b).

3.10 Two Electrode Fabrication of ASC Device

Figure 13 depicts the charge storage mechanism of fabricated asymmetric device. The working of an asymmetric supercapacitor (ASC) device made with synthesized GrM-$Bi_{1.8}Eu_{0.2}Mo_2O_9$ as the positive electrode and activated carbon (AC) as the negative electrode was assessed in two electrode setups. Figure 14(a) illustrates the CV analysis of the 10% Eu: GrM-$Bi_2Mo_2O_9$ and AC electrodes in 3M KOH electrolyte solution. Cyclic voltammograms revealed the pseudocapacitive behavior of GrM-$Bi_{1.8}Eu_{0.2}Mo_2O_9$ and EDLC characteristics of activated carbon in the measured potential range of 0 to 0.5 eV and -1 to 0 eV, respectively. The potential window of the prepared asymmetric supercapacitor was maintained at 0 -1.5 V throughout the CV analysis. The mass balance of positive and negative electrodes was determined using the equation

$$\frac{m_+}{m_-} = \frac{(\Delta V_-)C_-}{(\Delta V_+)C_+} \quad (2)$$

Where m_+ and m_- represent the mass of material coated on positive and negative electrodes, C_+ and C_- represent the specific capacitance of the positive and negative electrodes, and ΔV_+ and ΔV_- correspond to the potential difference of the positive and negative electrodes, respectively .[70,71] Herein, 2 mg of active material (GrM-$Bi_{1.8}Eu_{0.2}Mo_2O_9$) was loaded on the positive electrode and

5 mg of activated carbon was employed on the negative electrode to analyse their electrochemical behaviour. Figure 14(b) presents the CV curves of GrM-$Bi_{1.8}Eu_{0.2}Mo_2O_9$ and the AC electrode, which are investigated with varying scan rates from 5 mVs^{-1} to 100 mVs^{-1} in KOH electrolyte solution. As the scan rate increases, the CV graph displays a regular shape with quick charge transfer and less CV curve deformity, representing the super-capacitive behavior. Figure 14(c) depicts the GCD curves of the prepared ASC device observed at different current densities in a potential range of 0-1.5 V. The resultant specific capacitance of the fabricated device is 192.67 F g^{-1} at a current density of A g^{-1}. The energy density and the power density are the factors that determine the efficiency of a supercapacitor device and can be calculated as follows[72]

$$\text{Energy density (E)} = \frac{C \times \Delta V^2}{7.2} \ (\text{W h kg}^{-1}) \quad (3)$$

$$\text{Power density (P)} = \frac{3600\ E}{\Delta t} \ (\text{W kg}^{-1}) \quad (4)$$

where ΔV is a potential window (V), Δt is the discharge time (s), and C is the specific capacitance (F g^{-1}) of the devices. Table 2 provides the results for the fabricated GrM-$Bi_{1.8}Eu_{0.2}Mo_2O_9$ - based asymmetric devices, such as discharge time, specific capacitance, energy density, and power density. ASC device's extended energy density was 60.21 W h K g^{-1} with a power density of 750 W kg^{-1} at a current density of 1 A g^{-1}. The asymmetric supercapacitor should exhibit high cycle stability, which is important for practical uses, so a Swagelok-style device was used to measure the stability behavior of fabricated ASC.[73] The prepared ASC device's stability was evaluated and shown in Figure 14(d). The observation reveals that the rapid kinetics of the electrode/electrolyte interaction lowered the initial stability. After some more cycles, the reaction rate stabilized, which resulted in the following stability. The active electrode achieved a columbic efficiency of 96.5% after 10,000 cycles and maintained a capacity retention rate of 76.9% at 5 A

g^{-1}. The Ragone plot for the fabricated GrM-$Bi_{1.8}Eu_{0.2}Mo_2O_9$ - based ASC in comparision with other literatures were depicted in Figure 15 and Table 3 gives the comparision of the present work with previously reported data. The results of this work demonstrate that 10% doping of europium to graphene-modified $Bi_2Mo_2O_9$ significantly improves the energy and power density and can be employed as an active electrode material for supercapacitor applications.

4. Conclusion

This work reports the effective gel matrix synthesis of pristine $Bi_2Mo_2O_9$, β-$Bi_{2-x}Eu_xMo_2O_9$ and graphene-modified GrM-β-$Bi_{2-x}Eu_xMo_2O_9$ as electrode materials for supercapacitor. The monoclinic structure and the formation of the synthesized materials were affirmed using XRD and Raman analysis. The elemental confirmation of as-synthesized samples was carried out using XPS analysis. The mesoporous structure of $Bi_2Mo_2O_9$ aids in better performance in the presence of many active sites.

The electrochemical characteristics of $Bi_2Mo_2O_9$, β-$Bi_{2-x}Eu_xMo_2O_9$ and graphene-modified GrM-β-$Bi_{2-x}Eu_xMo_2O_9$ were analyzed using CV, GCD and EIS in three electrode configurations. Among the synthesized materials, GrM-$Bi_{1.8}Eu_{0.2}Mo_2O_9$ exhibits a maximum specific capacitance of about 904 F g^{-1} at 1 A g^{-1}. The capacitive retention of 10% Eu: GrM-$Bi_{1.8}Eu_{0.2}Mo_2O_9$ is 82.14% at 5 A g^{-1} after consecutive 5000 charge – discharge cycles. An asymmetric supercapacitor device fabricated with GrM-$Bi_{1.8}Eu_{0.2}Mo_2O_9$, investigated in two electrode configurations, shows a specific capacitance of 192.67 F g^{-1} at 1 A g^{-1} with the cyclic stability of 76.9 % at 5 A g^{-1} after 10000 cycles. The fabricated device's Energy and power density are 60.21 W h K g^{-1} and 750 W Kg^{-1}, respectively, at a current density of 1 A g^{-1}. In brief, the effect of Eu^{3+}, along with the modifications of graphene, greatly influenced the electrochemical performance, making them a suitable electrode material for supercapacitor application.

Declaration of competing interest

The authors declare that they have no conflict of interest and have no relevant financial or non-financial interests to disclose.

Author Contributions

All the authors contributed to the study's conception and design. Materials preparation, data collection, and analysis were performed by Jesman Sthevan Kovil Pitchai, Bagavathy Shunmughananthan, Priyadharshini Shanmugam, Govarthini Seerangan Selvam, Alagar Muthukaruppan, Thangaraju Dheivasigamani and Sivakumar Periyasamy. All authors read and approved the final manuscript.

Acknowledgement

The Authors sincerely thank the DST-FIST sponsored Instrumentation Center (File No: SR/FST/COLLEGE/2018/485) of Thanthai Periyar Government Arts and Science College (A), Tiruchirappalli – 23. The authors thank the Archbishop Casimir Instrumentation Centre of St. Joseph's College, Tiruchirappalli-620002. Authors Bagavathy Shunmughananthan, Priyadharshini Shanmugam and Govarthini Seerangan Selvam extends gratidue to PSG management for providing PSG iTech fulltime research scholarship.

References

[1] B.E. Conway, Electrochemical Supercapacitors Scientific Fundamentals and Technological Applications, 1999.

[2] M. Winter, R.J. Brodd, What are batteries, fuel cells, and supercapacitors?, Chem. Rev. 104 (2004) 4245–4269. https://doi.org/10.1021/cr020730k.

[3] F. Díaz-González, A. Sumper, O. Gomis-Bellmunt, R. Villafáfila-Robles, A review of energy storage technologies for wind power applications, Renew. Sustain. Energy Rev. 16

(2012) 2154–2171. https://doi.org/10.1016/j.rser.2012.01.029.

[4] S. Cao, H. Zhang, Y. Zhao, Y. Zhao, Pillararene/Calixarene-based systems for battery and supercapacitor applications, EScience. 1 (2021) 28–43. https://doi.org/10.1016/j.esci.2021.10.001.

[5] J. Cao, A. Emadi, A new battery/ultracapacitor hybrid energy storage system for electric, hybrid, and plug-in hybrid electric vehicles, IEEE Trans. Power Electron. 27 (2012) 122–132. https://doi.org/10.1109/TPEL.2011.2151206.

[6] S.F. Tie, C.W. Tan, A review of energy sources and energy management system in electric vehicles, Renew. Sustain. Energy Rev. 20 (2013) 82–102. https://doi.org/10.1016/j.rser.2012.11.077.

[7] A. Burk, Ultracapacitors: why, how, and where is the technology, J. Power Sources. 91 (2000) 37–50.

[8] S. Chu, Y. Cui, N. Liu, The path towards sustainable energy, Nat. Mater. 16 (2016) 16–22. https://doi.org/10.1038/nmat4834.

[9] W. Raza, F. Ali, N. Raza, Y. Luo, K.H. Kim, J. Yang, S. Kumar, A. Mehmood, E.E. Kwon, Recent advancements in supercapacitor technology, Nano Energy. 52 (2018) 441–473. https://doi.org/10.1016/j.nanoen.2018.08.013.

[10] S. Chu, A. Majumdar, Opportunities and challenges for a sustainable energy future, Nature. 488 (2012) 294–303. https://doi.org/10.1038/nature11475.

[11] C. Xiong, T. Wang, L. Zhou, Y. Zhang, L. Dai, Q. Zhou, Y. Ni, Fabrication of dual-function conductive cellulose-based composites with layered conductive network structures for supercapacitors and electromagnetic shielding, Chem. Eng. J. 472 (2023) 144958. https://doi.org/https://doi.org/10.1016/j.cej.2023.144958.

[12] W. Zhang, Z. Shahnavaz, X. Yan, X. Huang, S. Wu, H. Chen, J. Pan, T. Li, J. Wang, One-Step Solvothermal Synthesis of Raspberry-like NiCo-MOF for High-Performance Flexible Supercapacitors for a Wide Operation Temperature Range, Inorg. Chem. 61 (2022) 15287–15301. https://doi.org/10.1021/acs.inorgchem.2c02916.

[13] T. Brousse, D. Bélanger, K. Chiba, M. Egashira, F. Favier, J. Long, J.R. Miller, M. Morita, K. Naoi, P. Simon, W. Sugimoto, Materials for electrochemical capacitors, Springer Handbooks. (2017) 495–561. https://doi.org/10.1007/978-3-662-46657-5_16.

[14] L. Zhang, X.S. Zhao, Carbon-based materials as supercapacitor electrodes, Chem. Soc. Rev. 38 (2009) 2520–2531. https://doi.org/10.1039/b813846j.

[15] C. Xiong, T. Wang, J. Han, Z. Zhang, Y. Ni, Recent Research Progress of Paper-Based Supercapacitors Based on Cellulose, Energy Environ. Mater. (2023) e12651. https://doi.org/10.1002/eem2.12651.

[16] S. Najib, E. Erdem, Current progress achieved in novel materials for supercapacitor electrodes: Mini review, Nanoscale Adv. 1 (2019) 2817–2827. https://doi.org/10.1039/c9na00345b.

[17] U. Alam, A. Khan, D. Ali, D. Bahnemann, M. Muneer, Comparative photocatalytic activity of sol-gel derived rare earth metal (La, Nd, Sm and Dy)-doped ZnO photocatalysts for degradation of dyes, RSC Adv. 8 (2018) 17582–17594. https://doi.org/10.1039/c8ra01638k.

[18] Y. Wang, J. Guo, T. Wang, J. Shao, D. Wang, Y.W. Yang, Mesoporous transition metal oxides for supercapacitors, Nanomaterials. 5 (2015) 1667–1689. https://doi.org/10.3390/nano5041667.

[19] W. Yin, S. Hao, H. Cao, Solvothermal synthesis of magnetic CoFe2O4/rGO nanocomposites for highly efficient dye removal in wastewater, RSC Adv. 7 (2017) 4062–4069. https://doi.org/10.1039/c6ra26948f.

[20] F. Han, V.S.R. Kambala, M. Srinivasan, D. Rajarathnam, R. Naidu, Tailored titanium dioxide photocatalysts for the degradation of organic dyes in wastewater treatment: A review, Appl. Catal. A Gen. 359 (2009) 25–40. https://doi.org/10.1016/j.apcata.2009.02.043.

[21] Z. Wu, Y. Zhu, X. Ji, C.E. Banks, Transition Metal Oxides as Supercapacitor Materials, 2016. https://doi.org/10.1007/978-3-319-26082-2_9.

[22] W. Deng, X. Ji, Q. Chen, C.E. Banks, Electrochemical capacitors utilising transition metal

oxides: An update of recent developments, RSC Adv. 1 (2011) 1171–1178. https://doi.org/10.1039/c1ra00664a.

[23] L. Yang, C. Du, S. Tan, Z. Zhang, J. Song, Y. Su, Y. Zhang, S. Wang, G. Yu, H. Chen, L. Zhou, J. Chen, Improved photocatalytic properties of Fe(III) ion doped Bi2MoO6 for the oxidation of organic pollutants, Ceram. Int. 47 (2021) 5786–5794. https://doi.org/10.1016/j.ceramint.2020.10.165.

[24] Y. Zhang, L. Li, H. Su, W. Huang, X. Dong, Binary metal oxide: Advanced energy storage materials in supercapacitors, J. Mater. Chem. A. 3 (2015) 43–59. https://doi.org/10.1039/c4ta04996a.

[25] K. Zhang, L. Tong, Y. Ma, J. Wang, Z. Xia, Y. Han, Modulated up-conversion luminescence and low-temperature sensing of Gd3Ga5O12:Yb3+/Er3+ by incorporation of Fe3+ ions, J. Alloys Compd. 781 (2019) 467–472. https://doi.org/10.1016/j.jallcom.2018.12.147.

[26] T. Zhang, J. Huang, S. Zhou, H. Ouyang, L. Cao, A. Li, Microwave hydrothermal synthesis and optical properties of flower-like Bi2MoO6 crystallites, Ceram. Int. 39 (2013) 7391–7394. https://doi.org/10.1016/j.ceramint.2013.02.079.

[27] N. Devi, S.S. Ray, Performance of bismuth-based materials for supercapacitor applications: A review, Mater. Today Commun. 25 (2020) 101691. https://doi.org/10.1016/j.mtcomm.2020.101691.

[28] R. Kumar, A. Sudhaik, P. Raizada, A. Hosseini-Bandegharaei, V.K. Thakur, A. Saini, V. Saini, P. Singh, An overview on bismuth molybdate based photocatalytic systems: Controlled morphology and enhancement strategies for photocatalytic water purification, J. Environ. Chem. Eng. 8 (2020) 104291. https://doi.org/10.1016/j.jece.2020.104291.

[29] I. Matsuura, R. Schut, K. Hirakawa, The surface structure of the active bismuth molybdate catalyst, J. Catal. 63 (1980) 152–166. https://doi.org/10.1016/0021-9517(80)90068-8.

[30] H.H. Li, K.W. Li, H. Wang, Hydrothermal synthesis and photocatalytic properties of bismuth molybdate materials, Mater. Chem. Phys. 116 (2009) 134–142. https://doi.org/10.1016/j.matchemphys.2009.02.058.

[31] P.A. Batist, J.F.H. Bouwens, G.C.A. Schuit, Bismuth molybdate catalysts. Preparation, characterization and activity of different compounds in the BiMoO system, J. Catal. 25 (1972) 1–11. https://doi.org/10.1016/0021-9517(72)90196-0.

[32] Z.R. Khan, M. Shkir, T. Alshahrani, M.A. Manthrammel, S. AlFaify, Facile microwave synthesis of bismuth molybdate nanostructures and their characterization for optoelectronic applications, Solid State Sci. 107 (2020) 106361. https://doi.org/10.1016/j.solidstatesciences.2020.106361.

[33] W.H. Yang, Z.C. Ni, D. You, J.Y. Hou, B.N. Deng, R.W. Huang, S.G. Sun, J.B. Zhao, X. Li, Y.Y. Zhang, Y.J. Zhang, Multifunctional sulfur-immobilizing GO/MXene aerogels for highly-stable and long-cycle-life lithium–sulfur batteries, Rare Met. 42 (2023) 2577–2591. https://doi.org/10.1007/s12598-023-02272-6.

[34] T. Wang, C. Xiong, Y. Zhang, B. Wang, Q. Xiong, M. Zhao, Y. Ni, Multi-layer hierarchical cellulose nanofibers/carbon nanotubes/vinasse activated carbon composite materials for supercapacitors and electromagnetic interference shielding, Nano Res. (2023). https://doi.org/10.1007/s12274-023-6145-5.

[35] X. Huang, Y. Zhu, X. Yan, W. Zhang, Z. Shahnavaz, S. Wu, H. Chen, J. Pan, T. Li, Elm-like hierarchical microstructure promotes NiCoO2/GO/CF as a competitive candidate for supercapacitors and microwave absorbers, Mater. Charact. 199 (2023) 112801. https://doi.org/https://doi.org/10.1016/j.matchar.2023.112801.

[36] Q. Meng, K. Cai, Y. Chen, L. Chen, Research progress on conducting polymer based supercapacitor electrode materials, Nano Energy. 36 (2017) 268–285. https://doi.org/10.1016/j.nanoen.2017.04.040.

[37] M.M. Sundaram, D. Appadoo, Traditional salt-in-water electrolyte: Vs. water-in-salt electrolyte with binary metal oxide for symmetric supercapacitors: Capacitive vs. faradaic, Dalt. Trans. 49 (2020) 11743–11755. https://doi.org/10.1039/d0dt01871f.

[38] M.S. Javed, A.J. Khan, S. Asim, S.S.A. Shah, T. Najam, S.H. Siyal, M.F. Tahir, Z. Zhao, W. Mai, Insights to pseudocapacitive charge storage of binary metal-oxide nanobelts decorated activated carbon cloth for highly-flexible hybrid-supercapacitors, J. Energy

Storage. 31 (2020) 101602. https://doi.org/10.1016/j.est.2020.101602.

[39] W.H. Low, P.S. Khiew, S.S. Lim, C.W. Siong, E.R. Ezeigwe, Recent development of mixed transition metal oxide and graphene/mixed transition metal oxide based hybrid nanostructures for advanced supercapacitors, J. Alloys Compd. 775 (2019) 1324–1356. https://doi.org/10.1016/j.jallcom.2018.10.102.

[40] M. Isacfranklin, R. Yuvakkumar, G. Ravi, S.I. Hong, D. Velauthapillai, M. Thambidurai, C. Dang, T.S. Algarni, A.M. Al-Mohaimeed, Heterostructured SmCoO3/rGO composite for high-energy hybrid supercapacitors, Carbon N. Y. 172 (2021) 613–623. https://doi.org/10.1016/j.carbon.2020.10.081.

[41] M. Isacfranklin, G. Ravi, R. Yuvakkumar, P. Kumar, D. Velauthapillai, B. Saravanakumar, M. Thambidurai, C. Dang, Urchin like NiCo2O4/rGO nanocomposite for high energy asymmetric storage applications, Ceram. Int. 46 (2020) 16291–16297. https://doi.org/10.1016/j.ceramint.2020.03.186.

[42] J. Sthevan Kovil Pitchai, T. Dheivasigamani, B. Shunmughananthan, R. Arunagiri, S. Periyasamy, Single-wall and graphene-modified multiwall wasp nest shaped Bi2Mo2O9 self-assembly for performance-enhanced asymmetric supercapacitor, J. Mater. Chem. C. 10 (2022) 16453–16464. https://doi.org/10.1039/d2tc03294e.

[43] N. Shaheen, M. Aadil, S. Zulfiqar, H. Sabeeh, P.O. Agboola, M.F. Warsi, M.F. Aly Aboud, I. Shakir, Fabrication of different conductive matrix supported binary metal oxides for supercapacitors applications, Ceram. Int. 47 (2021) 5273–5285. https://doi.org/10.1016/j.ceramint.2020.10.108.

[44] D. Thangaraju, A. Durairajan, D. Balaji, S. Moorthy Babu, Synthesis and characterization of monoclinic KGd(WO4) 2 particles for non-cubic transparent ceramics, Opt. Mater. (Amst). 35 (2013) 753–756. https://doi.org/10.1016/j.optmat.2012.09.018.

[45] D. Balaji, A. Durairajan, D.thangaraju, K. Kavi Rasu, S. Moorthy Babu, Investigation of structural and luminescent properties of Pr3+ activated CsGd(WO4)2 by sol-gel synthesis, Mater. Sci. Eng. B Solid-State Mater. Adv. Technol. 178 (2013) 762–767. https://doi.org/10.1016/j.mseb.2013.03.008.

[46] D. Thangaraju, A. Durairajan, D. Balaji, S. Moorthy Babu, Y. Hayakawa, SiO 2/KGd(WO 4) 2:Eu 3+ composite luminescent nanoparticles: Synthesis and characterization, Mater. Chem. Phys. 135 (2012) 1115–1121. https://doi.org/10.1016/j.matchemphys.2012.06.031.

[47] P. Shanmugam, T. Dheivasigamani, S. Moorthy Babu, M. Shkir, E. El Sayed Massoud, R. Marnadu, V.R. Minnam Reddy, A facile sol–gel synthesis and characterization of europium (Eu) doped β-Bi2Mo2O9 nanoparticles with remarkably enhanced photocatalytic activity for waste-water treatments, Inorg. Chem. Commun. 146 (2022) 110163. https://doi.org/10.1016/j.inoche.2022.110163.

[48] F.D. Hardcastle, I.E. Wachs, Molecular structure of molybdenum oxide in bismuth molybdates by Raman spectroscopy, J. Phys. Chem. 95 (1991) 10763–10772. https://doi.org/10.1021/j100179a045.

[49] K. Seevakan, A. Manikandan, P. Devendran, Y. Slimani, A. Baykal, T. Alagesan, Structural, magnetic and electrochemical characterizations of Bi2Mo2O9 nanoparticle for supercapacitor application, J. Magn. Magn. Mater. 486 (2019) 165254. https://doi.org/10.1016/j.jmmm.2019.165254.

[50] B. Shunmughananthan, T. Dheivasigamani, J. Sthevan Kovil Pitchai, S. Periyasamy, Performance comparison of distinct bismuth molybdate single phases for asymmetric supercapacitor applications, Dalt. Trans. 51 (2022) 15579–15592. https://doi.org/10.1039/d2dt02092k.

[51] T. Thilagavathi, D. Venugopal, D. Thangaraju, R. Marnadu, B. Palanivel, M. Imran, M. Shkir, M. Ubaidullah, S. AlFaify, A facile co-precipitation synthesis of novel WO3/NiWO4 nanocomposite with improved photocatalytic activity, Mater. Sci. Semicond. Process. 133 (2021) 105970. https://doi.org/10.1016/j.mssp.2021.105970.

[52] T. Thilagavathi, D. Venugopal, R. Marnadu, J. Chandrasekaran, D. Thangaraju, B. Palanivel, M.S. Hamdy, M. Shkir, H.E. Ali, WO3/CoWO4 nanocomposite synthesis using a facile co-precipitation method for enhanced photocatalytic applications, J. Phys. Chem. Solids. 154 (2021) 110066. https://doi.org/10.1016/j.jpcs.2021.110066.

[53] N. Prakash, D. Thangaraju, R. Karthikeyan, M. Arivanandhan, Y. Shimura, Y. Hayakawa,

UV-visible and near-infrared active NaGdF4:Yb:Er/Ag/TiO2 nanocomposite for enhanced photocatalytic applications, RSC Adv. 6 (2016) 80655–80665. https://doi.org/10.1039/c6ra10208e.

[54] P. Forouzandeh, V. Kumaravel, S.C. Pillai, Electrode materials for supercapacitors: A review of recent advances, Catalysts. 10 (2020) 1–73. https://doi.org/10.3390/catal10090969.

[55] S. Asaithambi, P. Sakthivel, M. Karuppaiah, K. Balamurugan, R. Yuvakkumar, M. Thambidurai, G. Ravi, Synthesis and characterization of various transition metals doped SnO2@MoS2 composites for supercapacitor and photocatalytic applications, J. Alloys Compd. 853 (2021) 157060. https://doi.org/10.1016/j.jallcom.2020.157060.

[56] J. Wang, L. Wang, S. Zhang, S. Liang, X. Liang, H. Huang, W. Zhou, J. Guo, Facile synthesis of iron-doped SnO2/reduced graphene oxide composite as high-performance anode material for lithium-ion batteries, J. Alloys Compd. 748 (2018) 1013–1021. https://doi.org/10.1016/j.jallcom.2018.03.155.

[57] J. Sakurai, Y. Nakanuma, S. Fukuda, A. Mitsuda, Y. Isikawa, Valence transition between Eu2+ state and Eu3+ state in EuxY1-xPd2Si2 and Eu xLa1-xPd2Si2, J. Phys. Soc. Japan. 72 (2003) 2046–2052. https://doi.org/10.1143/JPSJ.72.2046.

[58] M. Isacfranklin, R. Yuvakkumar, G. Ravi, D. Velauthapillai, Morphological evolution of carnation flower-like Cu2CoSnS4 battery-type electrodes, Mater. Adv. (2022) 6643–6655. https://doi.org/10.1039/d2ma00509c.

[59] M. Isacfranklin, R. Yuvakkumar, G. Ravi, D. Velauthapillai, M. Pannipara, A.G. Al-Sehemi, Superior supercapacitive performance of Cu2MnSnS4asymmetric devices, Nanoscale Adv. 3 (2021) 486–498. https://doi.org/10.1039/d0na00775g.

[60] P.H. Wang, T.L. Wang, W.C. Lin, H.Y. Lin, M.H. Lee, C.H. Yang, Enhanced supercapacitor performance using electropolymerization of self-doped polyaniline on carbon film, Nanomaterials. 8 (2018) 214. https://doi.org/10.3390/nano8040214.

[61] J.S. Kovil Pitchai, B. Shunmughananthan, T. Dheivasigamani, S. Periyasamy, Graphene-guided growth of rare earth-doped Bi2Mo2O9 nano self-assembly for enhanced

asymmetric supercapacitor device performance, Sustain. Energy Fuels. 7 (2023) 1522–1536. https://doi.org/10.1039/d2se01654k.

[62] X. Wang, Y. Yang, P. He, F. Zhang, J. Tang, Z. Guo, R. Que, Facile synthesis of MnO2@NiCo2O4 core–shell nanowires as good performance asymmetric supercapacitor, J. Mater. Sci. Mater. Electron. 31 (2020) 1355–1366. https://doi.org/10.1007/s10854-019-02649-3.

[63] J. Acharya, T.H. Ko, M.K. Seo, M.S. Khil, H.Y. Kim, B.S. Kim, Oxalic acid assisted rapid synthesis of mesoporous NiCo2O4 nanorods as electrode materials with higher energy density and cycle stability for high-performance asymmetric hybrid supercapacitor applications, J. Colloid Interface Sci. 564 (2020) 65–76. https://doi.org/10.1016/j.jcis.2019.12.098.

[64] H. Tong, Q. Meng, J. Liu, T. Li, D. Gong, J. Xiao, L. Shen, T. Zhang, D. Bing, X. Zhang, Cross-linked NiCo2O4 nanosheets with low crystallinity and rich oxygen vacancies for asymmetric supercapacitors, J. Alloys Compd. 822 (2020) 153689. https://doi.org/10.1016/j.jallcom.2020.153689.

[65] T.A. Raja, P. Vickraman, Role of dual redox additives KI/VOSO4 in manganese ammonium phosphate at graphene quantum dots for supercapattery, Int. J. Energy Res. 46 (2022) 9097–9113. https://doi.org/10.1002/er.7787.

[66] T. Arul Raja, P. Vickraman, A. Simon Justin, B. Joji Reddy, Microwave Synthesis of Zinc Ammonium Phosphate/Reduced Graphene Oxide Hybrid Composite for High Energy Density Supercapacitors, Phys. Status Solidi Appl. Mater. Sci. 217 (2020). https://doi.org/10.1002/pssa.201900736.

[67] M. Isacfranklin, B.J. Rani, G. Ravi, R. Yuvakkumar, S.I. Hong, D. Velauthapillai, B. Saravanakumar, Hydrothermal Method–Derived MnMoO4 Crystals: Effect of Cationic Surfactant on Microstructures and Electrochemical Properties, ChemistrySelect. 5 (2020) 7728–7733. https://doi.org/10.1002/slct.202001384.

[68] W. Ma, H. Nan, Z. Gu, B. Geng, X. Zhang, Superior performance asymmetric supercapacitors based on ZnCo2O4@MnO2 core-shell electrode, J. Mater. Chem. A. 3

(2015) 5442–5448. https://doi.org/10.1039/c5ta00012b.

[69] M. Wang, Y. Zhao, X. Zhang, R. Qi, S. Shi, Z. Li, Q. Wang, Y. Zhao, Interface-rich core-shell ammonium nickel cobalt phosphate for high-performance aqueous hybrid energy storage device without a depressed power density, Electrochim. Acta. 272 (2018) 184–191. https://doi.org/10.1016/j.electacta.2018.04.005.

[70] G.S. Selvam, T. Dheivasigamani, K. Ammasai, J.S.K. Pitchai, Lutetium Gallium Garnet (Lu3Ga5O12): A potential material for Supercapacitor and Pesticide detection applications, J. Alloys Compd. 973 (2023) 172842. https://doi.org/10.1016/j.jallcom.2023.172842.

[71] B. Shunmughananthan, T. Dheivasigamani, J. Sthevan Kovil Pitchai, Rare-earth gallium garnet (RE3Ga5O12, RE = Eu, Gd, Dy, Er, and Yb) self-assembled nanostructure based battery type electrodes for efficient asymmetric supercapacitor applications, J. Energy Storage. 73 (2023) 109092. https://doi.org/10.1016/j.est.2023.109092.

[72] S. Asaithambi, P. Sakthivel, M. Karuppaiah, R. Yuvakkumar, K. Balamurugan, T. Ahamad, M.A.M. Khan, G. Ramalingam, M.K.A. Mohammed, G. Ravi, Preparation of Fe-SnO2@CeO2 nanocomposite electrode for asymmetric supercapacitor device performance analysis, J. Energy Storage. 36 (2021) 102402.

[73] P. Shanmugam, T. Dheivasigamani, J.S. Kovil Pitchai, A. Muthukaruppan, Stable single phases of samarium gallium oxide (Sm3GaxOy) nano semiconductor self-assembly for supercapacitor and photocatalytic applications, Dalt. Trans. 52 (2023) 5366–5382. https://doi.org/10.1039/d3dt00261f.

[74] D. Ali, F. Ashiq, I. Muneer, H.M. Fahad, A. Waheed, M.Z. Butt, R. Ahmad, M.F.M.R. Wee, Bismuth iron manganese oxide nanocomposite for high performance asymmetric supercapacitor, Electrochim. Acta. 464 (2023) 142863. https://doi.org/https://doi.org/10.1016/j.electacta.2023.142863.

[75] F. Wu, X. Wang, W. zheng, H. Gao, C. Hao, C. Ge, Synthesis and characterization of hierarchical Bi2MoO6/Polyaniline nanocomposite for all-solid-state asymmetric supercapacitor, Electrochim. Acta. 245 (2017) 685–695.

https://doi.org/10.1016/j.electacta.2017.05.165.

[76] R. Rameshbabu, M. Sandhiya, M. Sathish, Fe (III) ions grafted bismuth oxychloride nanosheets for enhanced electrochemical supercapacitor application, J. Electroanal. Chem. 862 (2020) 113958. https://doi.org/10.1016/j.jelechem.2020.113958.

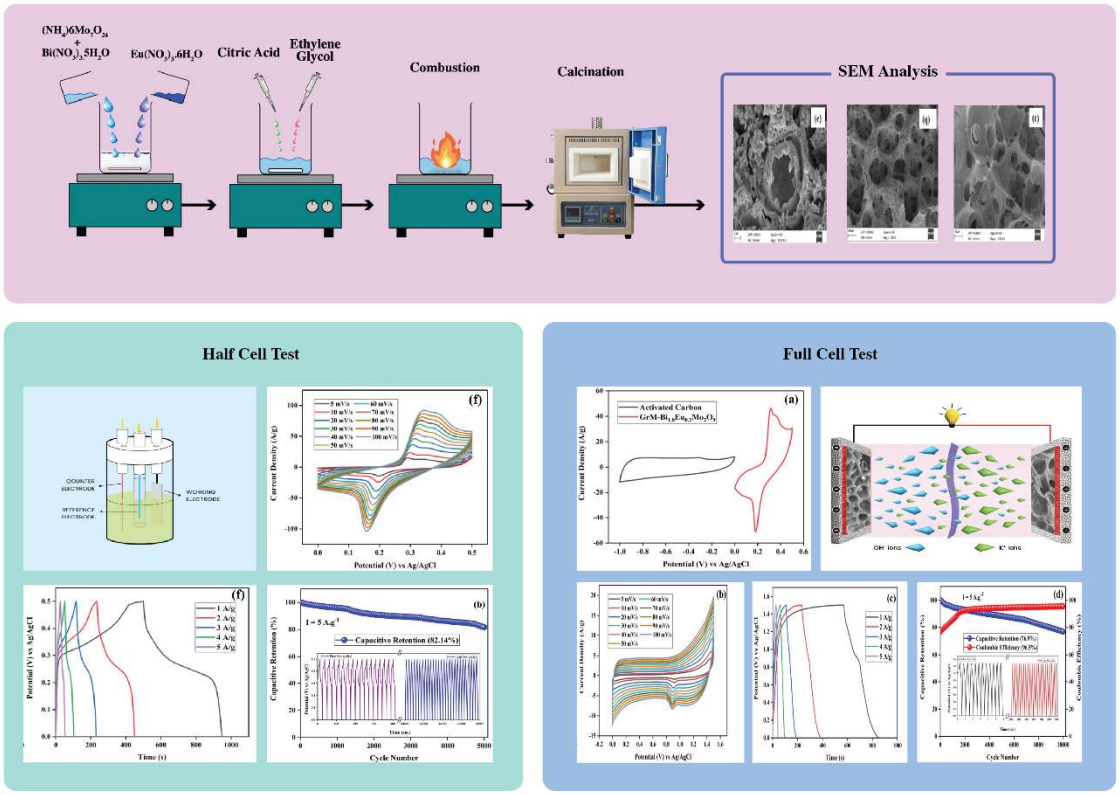

Figure 1. Graphical representation of as-synthesized materials for asymmetric supercapacitor application

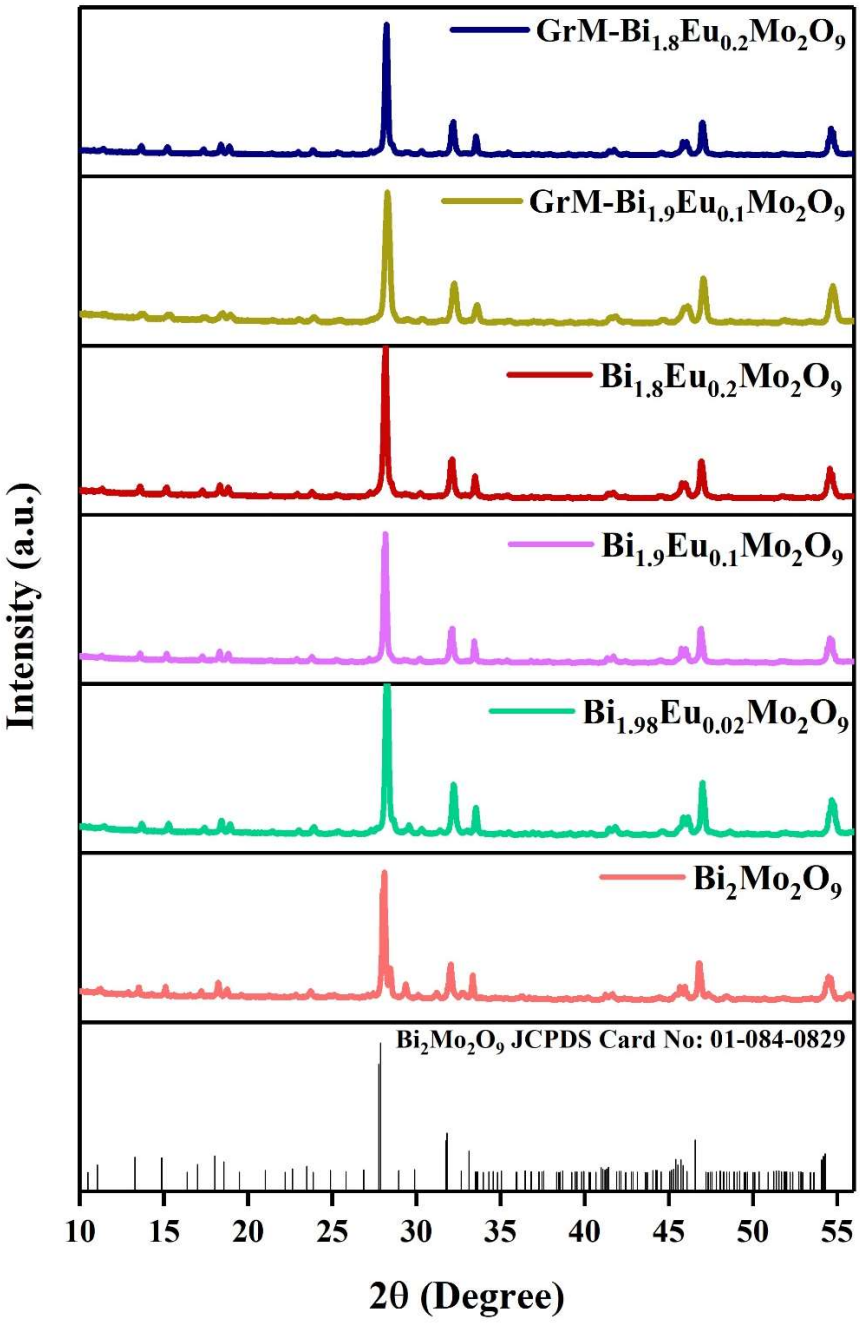

Figure 2. XRD patterns of as-synthesized $Bi_2Mo_2O_9$, $Bi_{2-x}Eu_xMo_2O_9$ and GrM -$Bi_{2-x}Eu_xMo_2O_9$

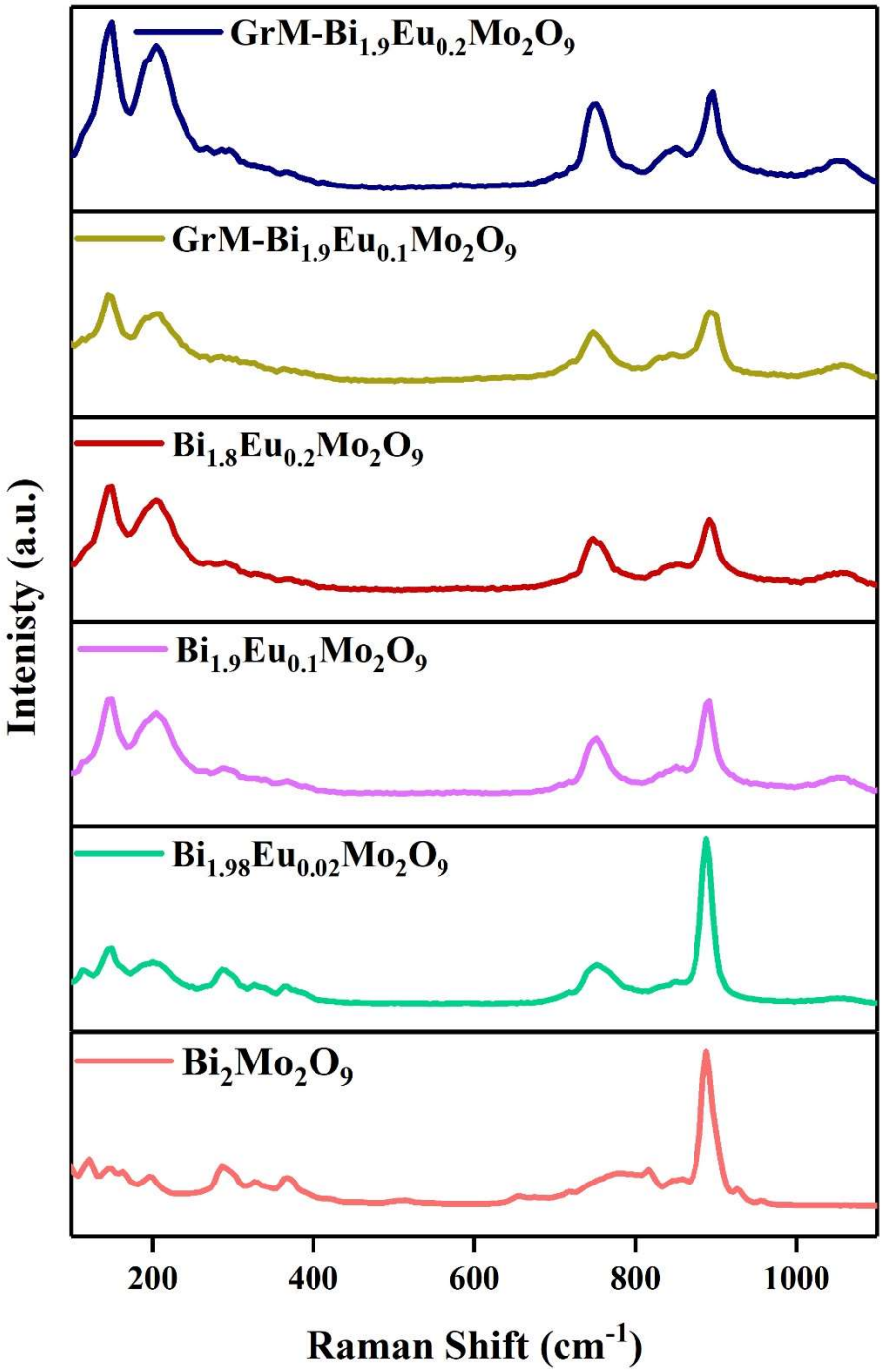

Figure 3. Comparative Raman spectra of $Bi_2Mo_2O_9$, $Bi_{2-x}Eu_xMo_2O_9$ and GrM -$Bi_{2-x}Eu_xMo_2O_9$

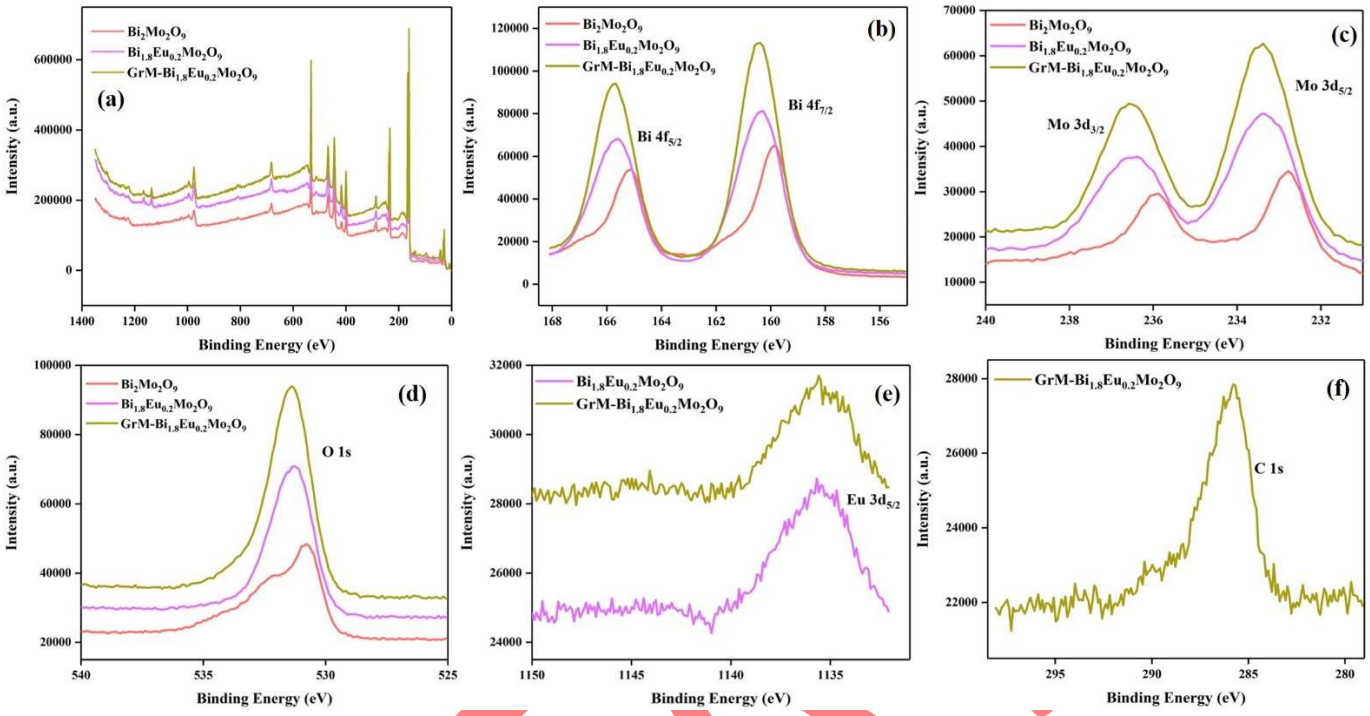

Figure 4. XPS survey spectrum (a), Bi 4f (b), Mo 3d (c), O 1s (d), Eu 3d (e) and C 1s (f) spectrum of $Bi_2Mo_2O_9$, $Bi_{1.8}Eu_{0.2}Mo_2O_9$ and GrM-$Bi_{1.8}Eu_{0.2}Mo_2O_9$.

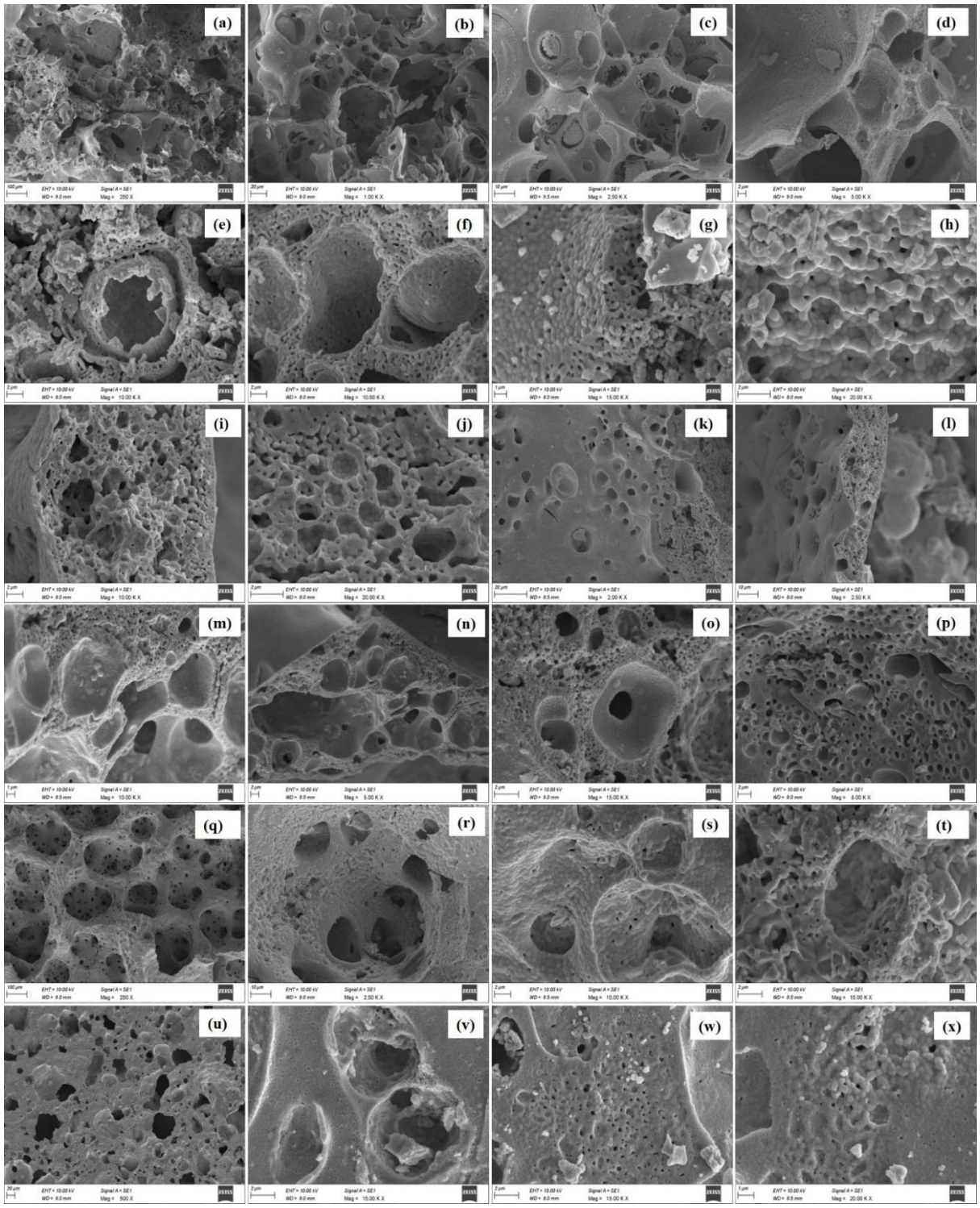

Figure 5. SEM micrographs of $Bi_2Mo_2O_9$ (a-d), $Bi_{1.98}Eu_{0.02}Mo_2O_9$ (e-h), $Bi_{1.9}Eu_{0.1}Mo_2O_9$ (i-l), $Bi_{1.8}Eu_{0.2}Mo_2O_9$ (m-p), GrM-$Bi_{1.9}Eu_{0.1}Mo_2O_9$ (q-t) and GrM-$Bi_{1.8}Eu_{0.2}Mo_2O_9$ (u-x).

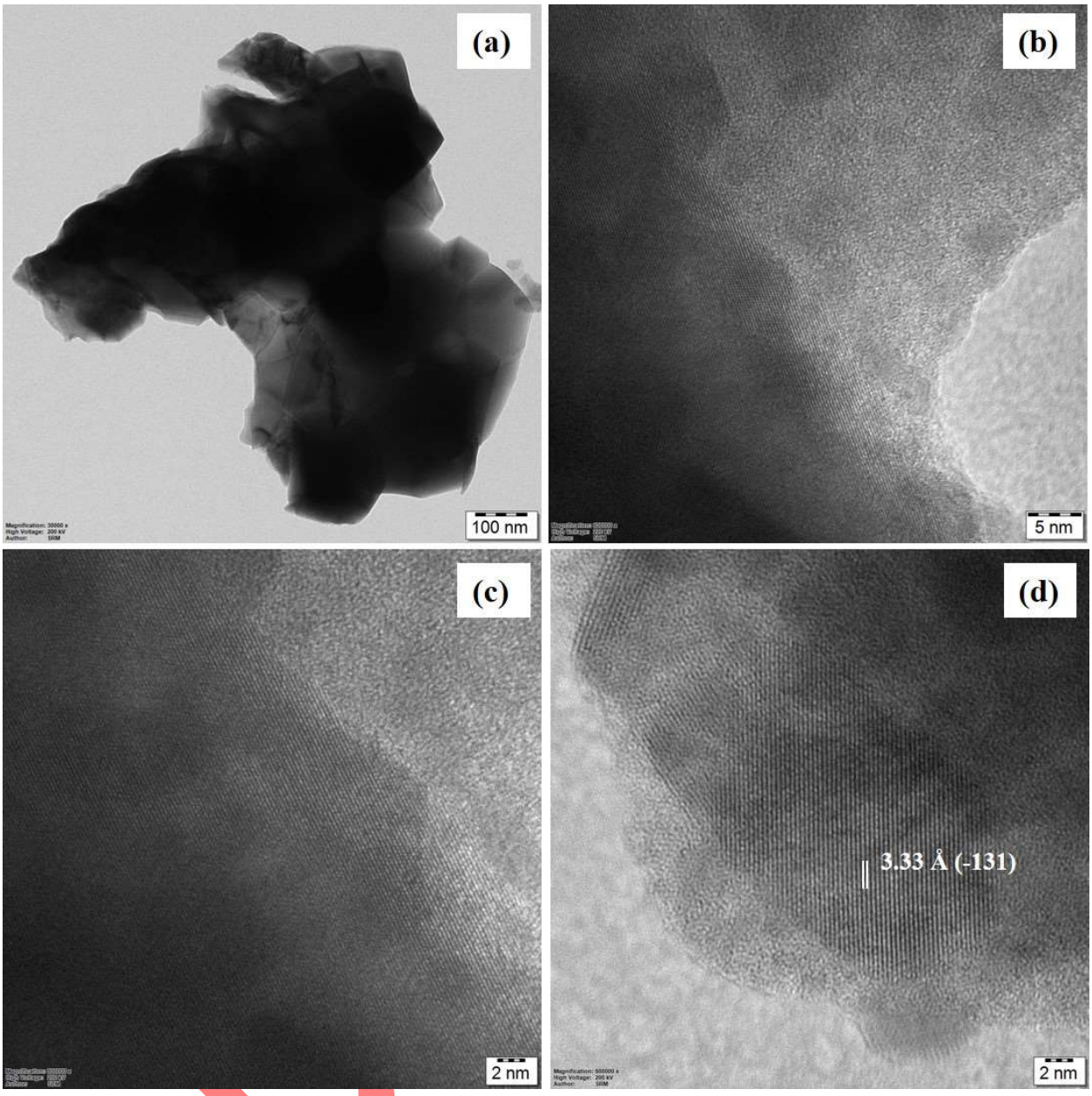

Figure 6. TEM analysis of GrM-$Bi_{1.8}Eu_{0.2}Mo_2O_9$

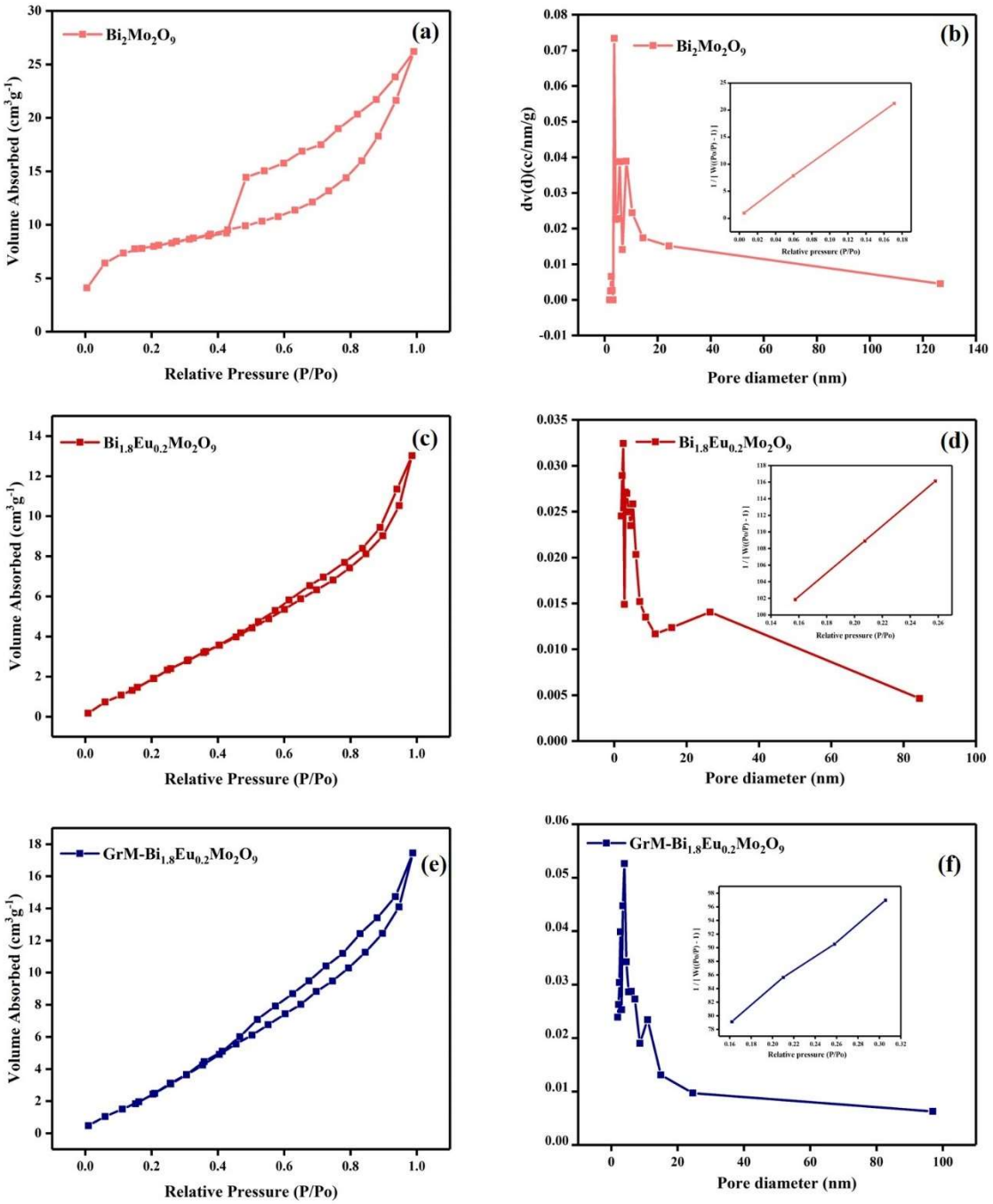

Figure 7. BET analysis of $Bi_2Mo_2O_9$, $Bi_{1.8}Eu_{0.2}Mo_2O_9$ and GrM-$Bi_{1.8}Eu_{0.2}Mo_2O_9$.

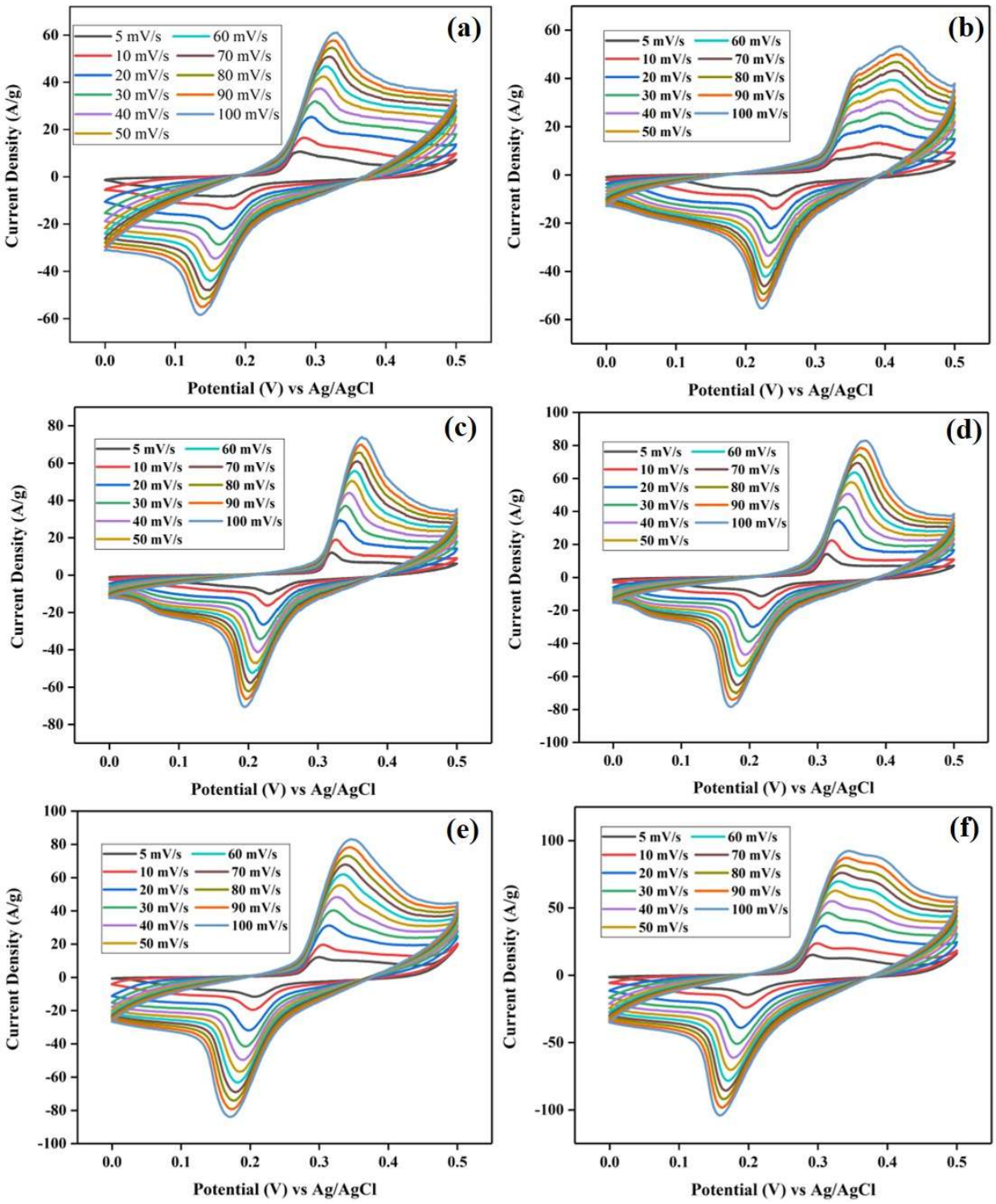

Figure 8. Cyclic voltammograms of (a) $Bi_2Mo_2O_9$, (b) $Bi_{1.98}Eu_{0.02}Mo_2O_9$, (c) $Bi_{1.9}Eu_{0.1}Mo_2O_9$, (d) $Bi_{1.8}Eu_{0.2}Mo_2O_9$, (e) GrM-$Bi_{1.9}Eu_{0.1}Mo_2O_9$ and (f) GrM-$Bi_{1.8}Eu_{0.2}Mo_2O_9$.

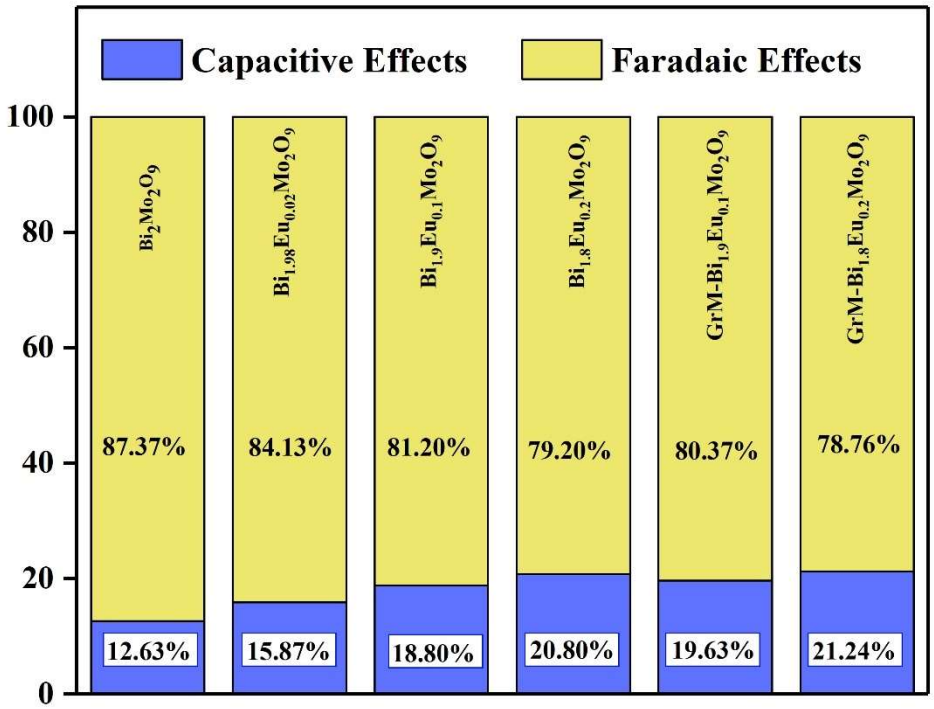

Figure 9. Diffusive and capacitive effect of $Bi_2Mo_2O_9$, $Bi_{1.98}Eu_{0.02}Mo_2O_9$, $Bi_{1.9}Eu_{0.1}Mo_2O_9$, $Bi_{1.8}Eu_{0.2}Mo_2O_9$, GrM-$Bi_{1.9}Eu_{0.1}Mo_2O_9$ and GrM-$Bi_{1.8}Eu_{0.2}Mo_2O_9$ using Trasatti method.

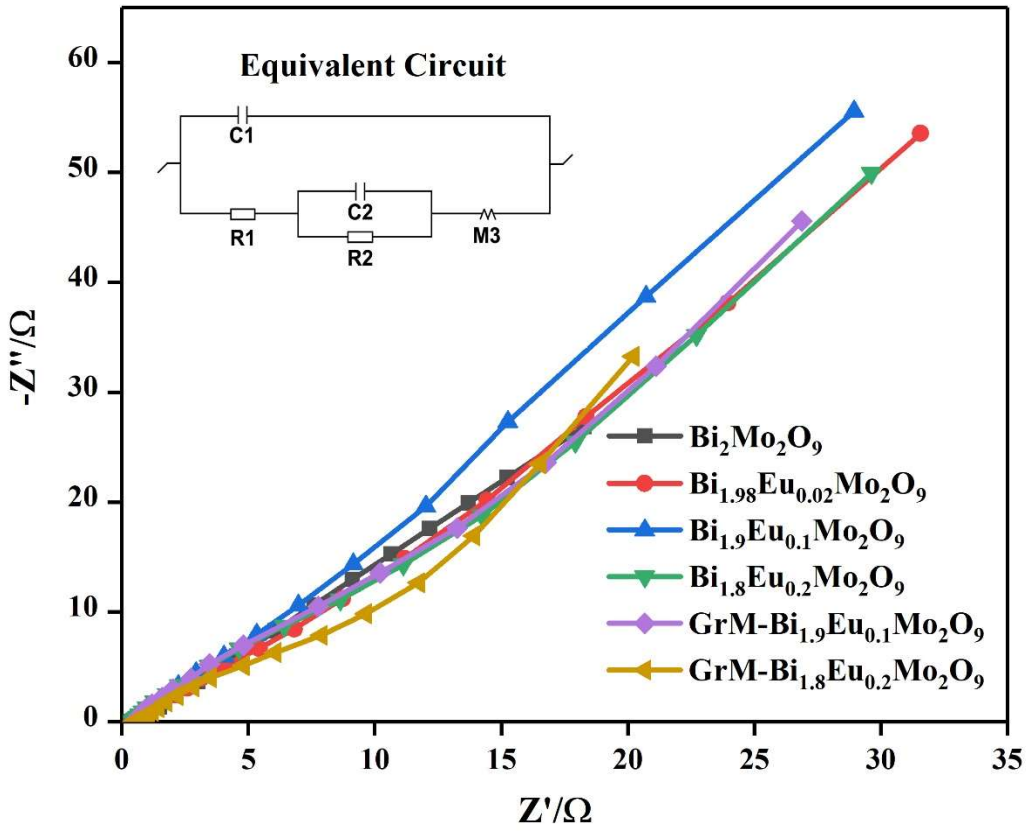

Figure 10. EIS spectra of synthesized materials.

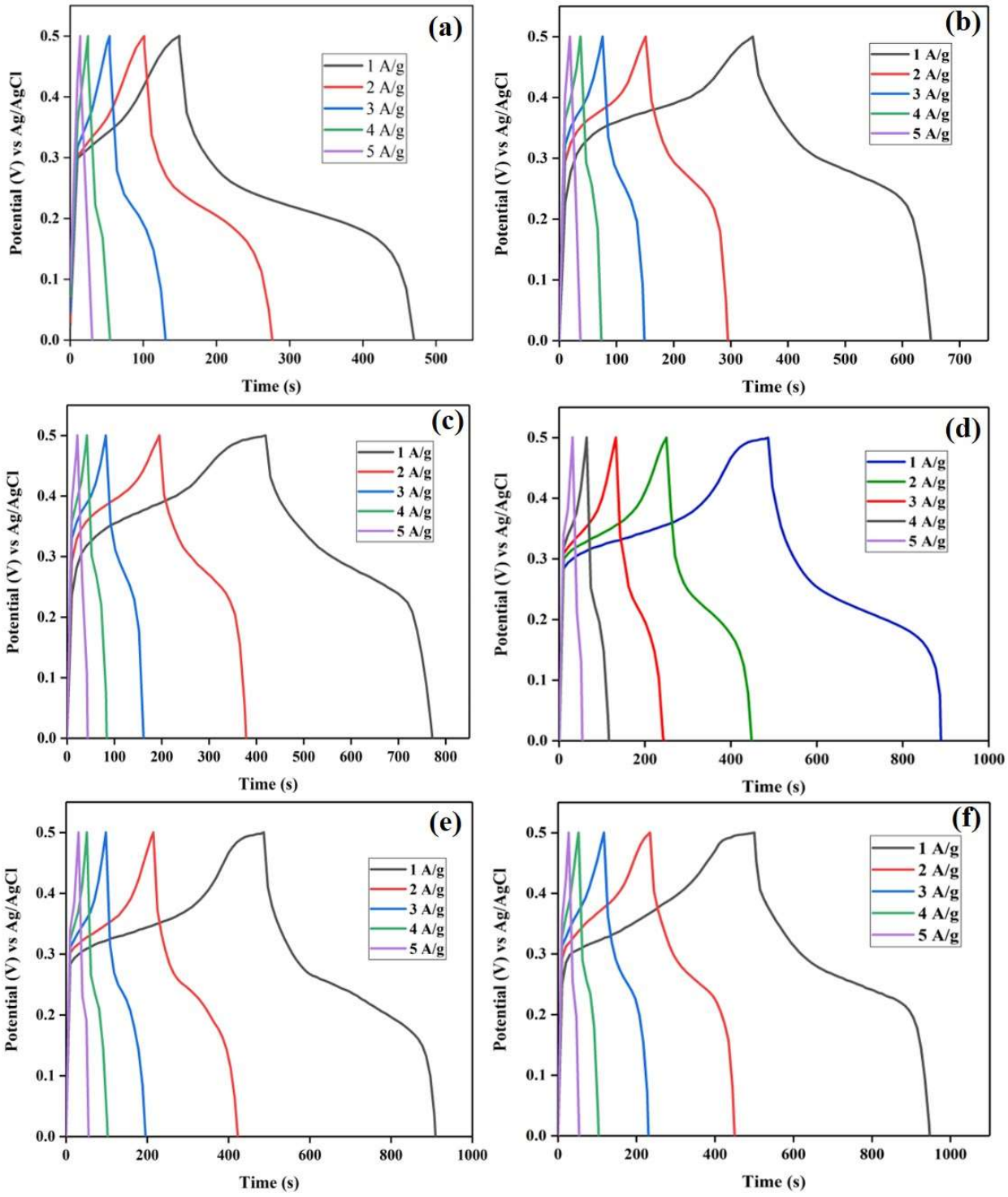

Figure 11. GCD curves of $Bi_2Mo_2O_9$ (a), $Bi_{1.98}Eu_{0.02}Mo_2O_9$ (b), $Bi_{1.9}Eu_{0.1}Mo_2O_9$ (c), $Bi_{1.8}Eu_{0.2}Mo_2O_9$ (d), GrM-$Bi_{1.9}Eu_{0.1}Mo_2O_9$ (e) and GrM-$Bi_{1.8}Eu_{0.2}Mo_2O_9$ (f).

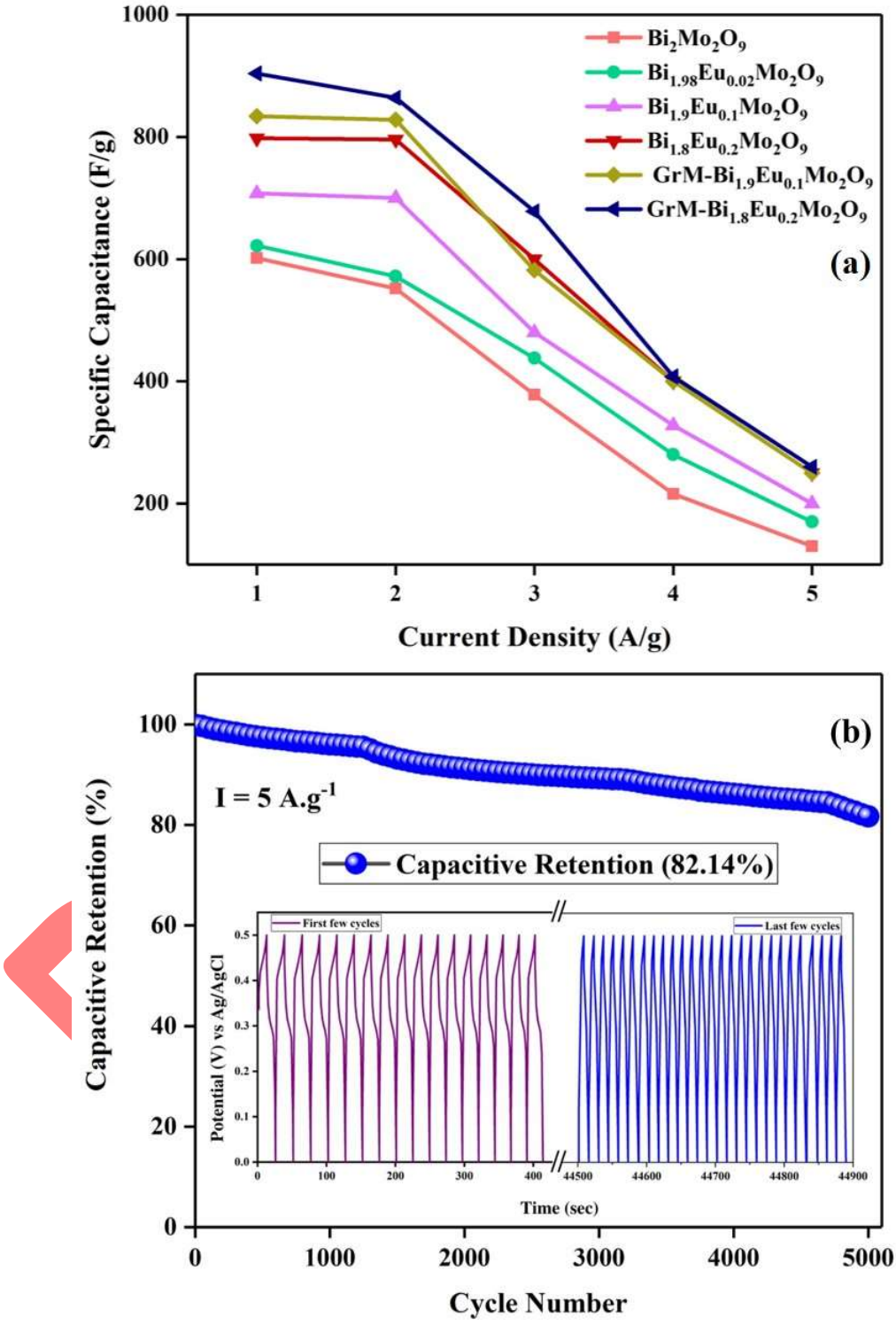

Figure 12. The comparison graph of specific capacitance with current density of the pristine materials (a) and the stability graph of GrM-$Bi_{1.8}Eu_{0.2}Mo_2O_9$ (b)

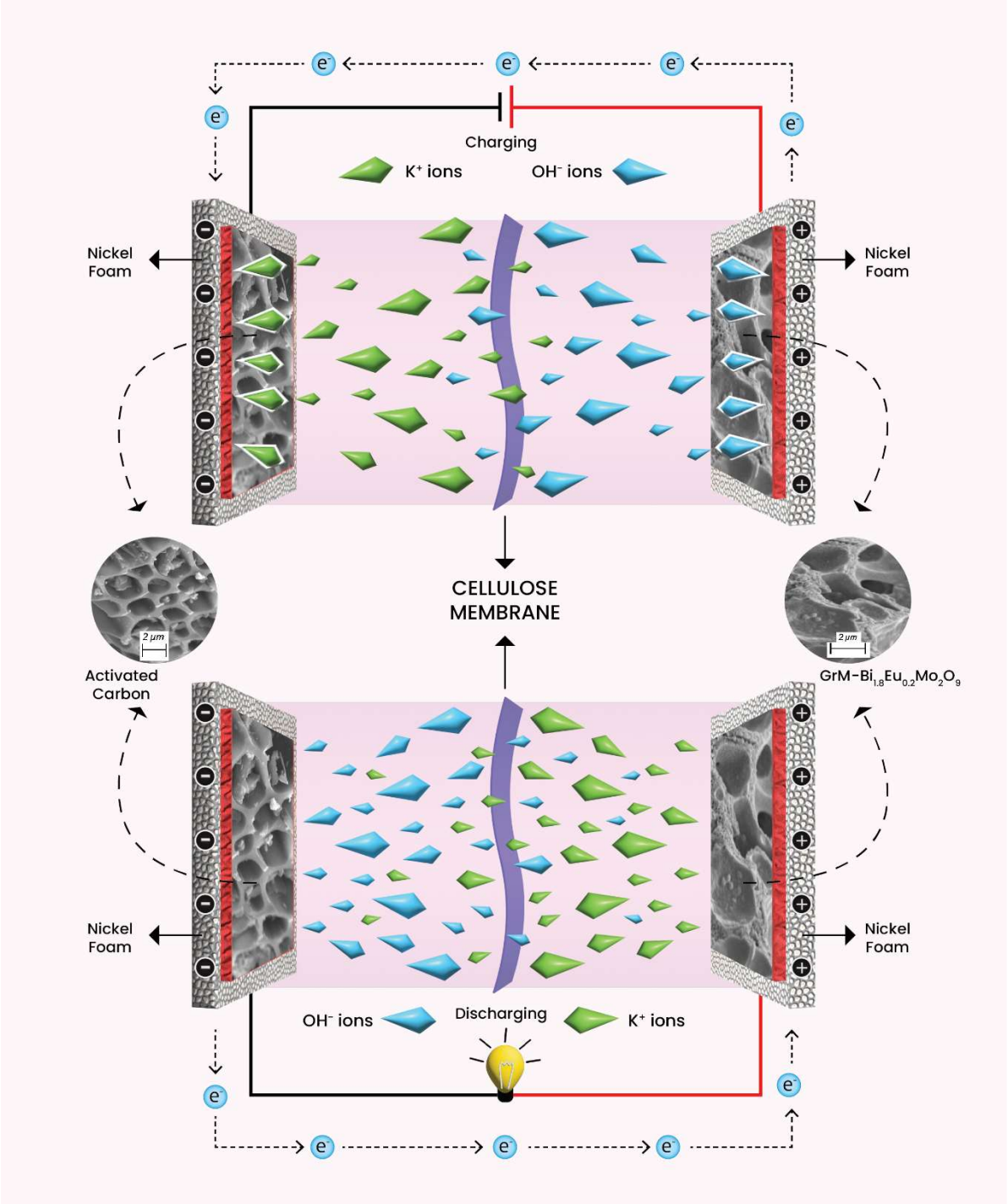

Figure 13. Charge storage mechanism of an asymmetric supercapacitor.

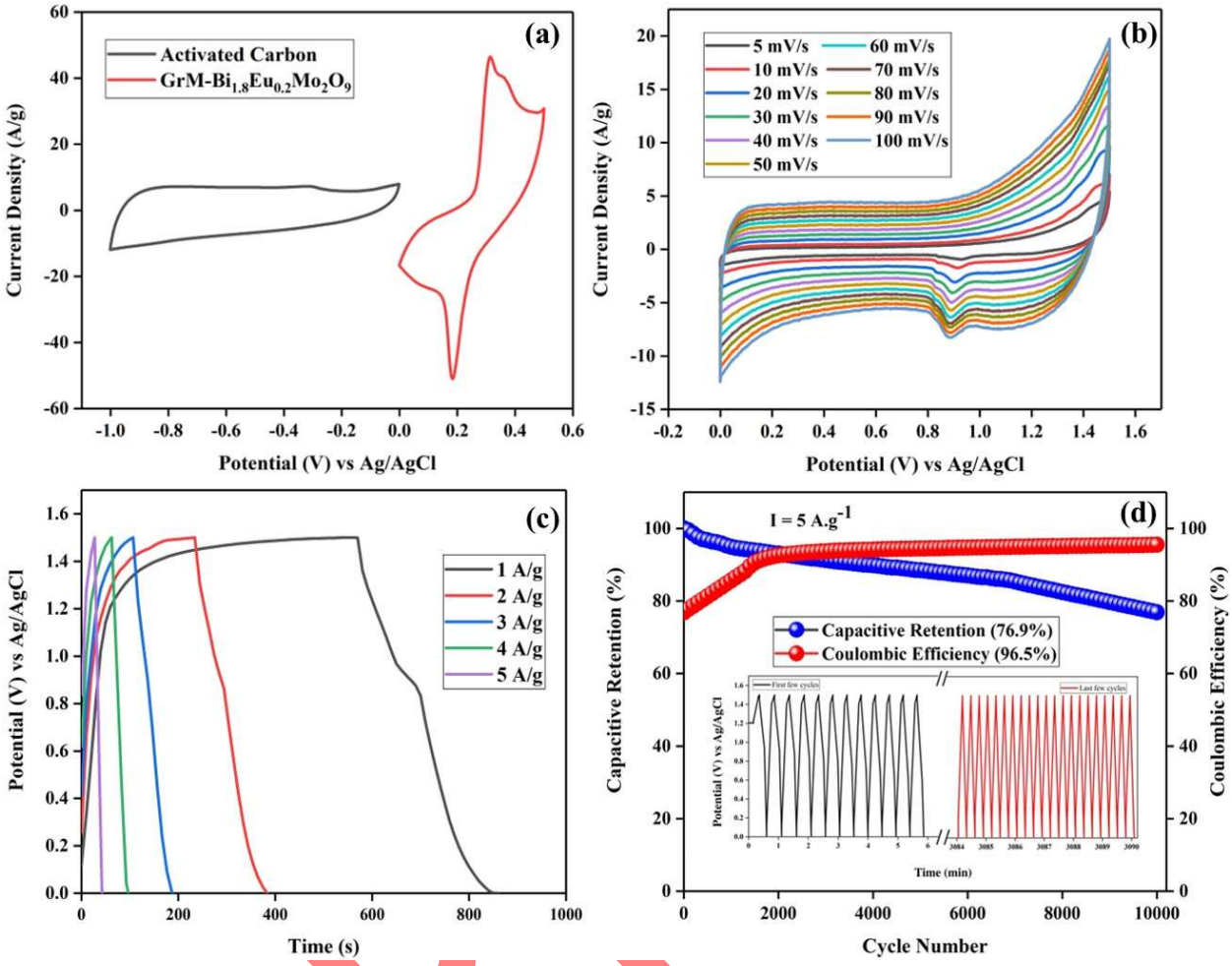

Figure 14. CV comparison of activated carbon and active material (a), CV graph (b), GCD curves (c) and capacitive retention of fabricated ASC device (d) using GrM-$Bi_{1.8}Eu_{0.2}Mo_2O_9$.

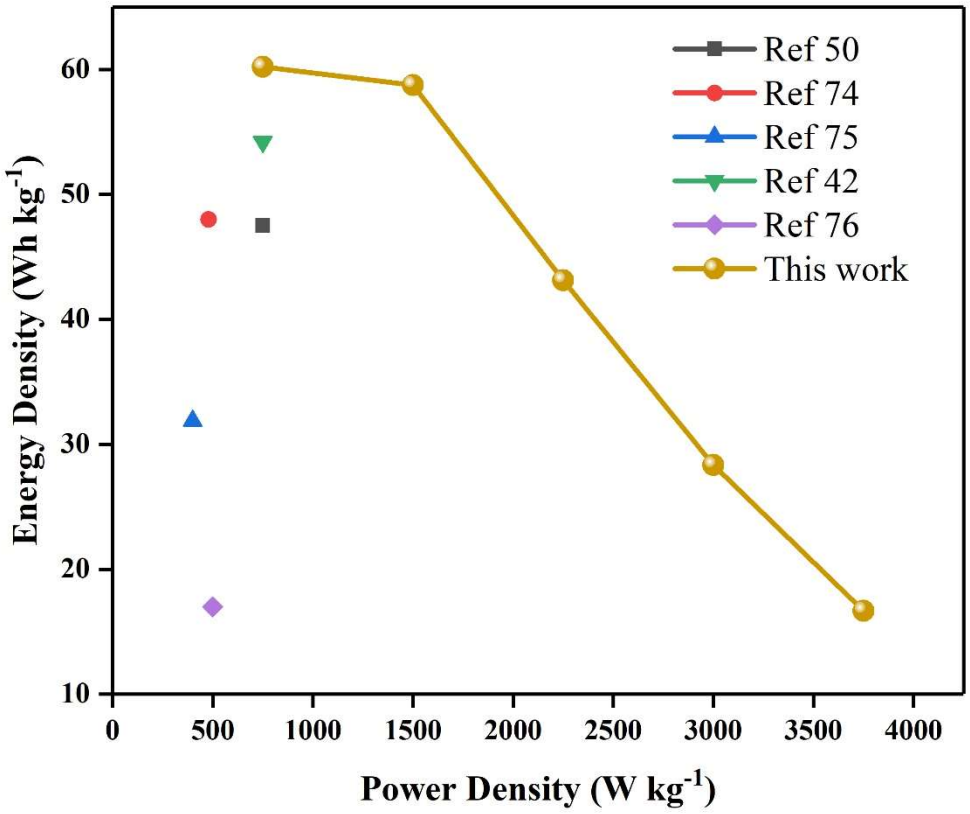

Figure 15. Ragone plot for fabricated ASC device with other literature reports.

Table 1: Series resistance (Rs) and charge transfer resistance (R_{CT}) obtained from EIS analysis.

Materials	Rs (Ω)	R_{CT} (Ω)	Peak current Density at 100 $mV.s^{-1}$ ($A.cm^{-1}$)
$Bi_2Mo_2O_9$	0.03305	1.858	52.54
$Bi_{1.98}Eu_{0.02}Mo_2O_9$	0.2519	1.544	53.28
$Bi_{1.9}Eu_{0.1}Mo_2O_9$	0.2673	0.9141	73.7
$Bi_{1.8}Eu_{0.2}Mo_2O_9$	0.6717	0.2424	83.3
GrM-$Bi_{1.9}Eu_{0.1}Mo_2O_9$	0.2676	0.8968	82.85
GrM-$Bi_{1.8}Eu_{0.2}Mo_2O_9$	0.3687	0.1358	92.1

Table 2: Electrochemical performance of fabricated ASC device.

Current Density ($A.g^{-1}$)	Discharge Time (s)	Potential Window (V)	Specific capacitance ($F.g^{-1}$)	Energy Density ($W.h.Kg^{-1}$)	Power Density ($W.Kg^{-1}$)
1	289	1.5	192.67	60.21	750
2	141	1.5	188	58.75	1500
3	69	1.5	138	43.12	2250
4	34	1.5	90.67	28.33	3000
5	16	1.5	53.33	16.67	3750

Table 3: ASC device comparision with previous literature.

Electrode Material	Synthesis Route	Electrolyte	Energy Density	Power Density	Cyclic Stability	Ref
$Bi_2Mo_3O_{12}$	Gel matrix	3M KOH	47.5 Wh kg^{-1}	750 W kg^{-1}	71.9% after 10000 cycles @ 5 Ag^{-1}	[50]
$Bi_2Fe_2Mn_2O_{10}$	Solgel/ Ultrasonic assisted coprecipitation	6M KOH	48 Wh kg^{-1}	480 W kg^{-1}	93.3% after 5000 cycles @ 0.6 Ag^{-1}	[74]
Bi_2MoO_6/PANI	Chemical polymerization	3M KOH	31.9 Wh kg^{-1}	400 W kg^{-1}	86.5% after 6000 cycles	[75]
Graphene modified M-$Bi_2Mo_2O_9$	Sol-gel auto combustion	3M KOH	54.2 Wh kg^{-1}	750 W kg^{-1}	74.28% after 10000 cycles @ 5 Ag^{-1}	[42]
Fe(III)/BiOCl	Solvothermal	1M H_2SO_4	17 Wh kg^{-1}	500 W kg^{-1}	99% after 5000 cycles @ 5 Ag^{-1}	[76]
GrM-$Bi_{1.8}Eu_{0.2}Mo_2O_9$	Sol-gel auto combustion	3M KOH	60.2 Wh kg^{-1}	750 W kg^{-1}	76.9% after 10000 cycles @ 5 Ag^{-1}	This work